Local and global sensitivity analysis of *Cr(VI)* geogenic leakage under uncertain environmental conditions

by, G. Ceriotti[a], L. Guadagnini[a], G. Porta[a] & A. Guadagnini[a,b]

[a] Department of Civil and Environmental Engineering, Politecnico di Milano, Piazza L. Da Vinci 32, 20133 Milano, Italy

[b] Department of Hydrology and Atmospheric Sciences, University of Arizona, Tucson, AZ 85721, USA

Corresponding author: Laura Guadagnini, laura.guadagnini@polimi.it, Department of Civil and Environmental Engineering, Politecnico di Milano, Piazza L. Da Vinci 32, 20133 Milano, Italy.

Abstract

We focus on the joint application of local and global sensitivity analyses (SA) to characterize propagation of model parameter uncertainties to outputs of subsurface water geochemical models. The latter typically involve uncertain inputs, including environmental conditions, mineral rock composition and flow/transport features. In this context, implementation of sensitivity analysis techniques enables us to grasp the relative role of each model input. Here, we focus on the application of several sensitivity approaches to the assessment of *Cr(VI)* geogenic leakage due to water-rock interactions. We specifically target the impact of uncertain environmental conditions on the chemical composition of spring waters following water transfer through a host rock system with given mineral composition. We employ a reaction path modeling approach and represent uncertainties of environmental conditions through three parameters, i.e., oxygen fugacity (f_{O2}), CO_2 fugacity (f_{CO2}), and temperature, which we consider as random quantities. We consider three diverse methodologies, i.e., (*a*) the Scatter Plots sensitivity analysis (SP) (*b*) the Distributed Evaluation of Local Sensitivity Analysis (DELSA); and (*c*) a moment-based global sensitivity analysis. Our results suggest that (*a*) the relative importance of a given model parameter in driving the uncertainty of the spring water composition may display remarkable variations across the sampled parameter space, and (*b*) parameter ranking through sensitivity metrics for geochemical applications in subsurface water resources requires a joint assessment of local and global sensitivity.

1 Introduction

Appropriate approaches to modeling of groundwater geochemistry can contribute to improved data-driven understanding of (field- and laboratory- scale) processes and long term behavior of geochemical systems (e.g., Bethke, 2007; Crawford, 1999). In this sense, geochemical models can be perceived as (intentionally) streamlined representations of reality (Crawford, 1999) and are subject to uncertainty. The latter stems from incomplete knowledge of the physics controlling the evolution of a real subsurface system and their transposition into mathematical formulations, as well as from difficulties of properly defining and characterizing input parameters embedded in such mathematical models (e.g., Bethke, 2007; Neuman, 2003a, 2003b; Tartakovsky, 2013; Ye et al., 2005; Zhu & Anderson, 2002 and references therein). Parameter estimation is typically performed, in an inverse problem framework, through model calibration against data sampled in field or laboratory settings (e.g. Carrera & Neuman, 1986; Dai & Samper, 2004; Yang et al., 2014), a procedure that can be demanding and expensive, especially when dealing with subsurface systems. In this broad context, identifying priorities for the characterization of model parameters and optimizing data acquisition during sampling campaigns for model application should be considered as critical elements associated with modern geochemical model developments and engineering within an application-oriented framework. Robust sensitivity analyses and uncertainty quantification for a given model are key to accomplish these objectives (e.g., Iooss & Lamaitre, 2015; Razavi & Gupta, 2015; Saltelli et al., 2008 and references therein).

A variety of approaches to sensitivity analysis have been proposed. These are essentially framed within the context of local or global sensitivity analysis. Local sensitivity analysis (LSA) techniques allow quantifying the sensitivity of a model output to small perturbations of input parameter values. Results of such analyses are informative of the system behavior in the proximity of the perturbed input parameter value (Razavi & Gupta, 2015; Saltelli et al., 2005). Otherwise, global sensitivity analysis (GSA) approaches provide a general framework to characterize sensitivities of model outputs across the

entire (user-defined) range of variability of model input parameters (e.g., Dell'Oca et al., 2017; Razavi & Gupta, 2015). GSA approaches are relatively recent, as compared to LSA analyses, and have already found promising implementations in diverse fields of environmental and Earth sciences (e.g., Ciriello et al., 2013a, 2013b, 2015; Dell'Oca et al., 2017; Formaggia et al., 2013; Riva et al., 2015; Saltelli et al., 2008). While many studies confined to LSA approaches implementation on chemical and geochemical models can be found in the literature (see Saltelli et al., 2005, 2012 and reference therein), an increasing interest into GSA approaches in chemistry and geochemistry has been recorded in the last decade (Ferretti et al., 2016).

In this study we analyze the way the implementation of a variety of sensitivity analysis tools (local and global) can assist quantification of (*a*) the relative importance of uncertain model parameters and (*b*) the ensuing uncertainty of model outputs in the context of relevant environmental geochemical scenarios. As a test bed, we target the occurrence of hexavalent chromium (*Cr(VI)*) in spring water associated with fractured and partially altered ophiolitic rock settings. The latter stands as a scenario of concern in the framework of studies aimed at identifying natural background levels of given chemicals in groundwater bodies (e.g., Runnells et al., 1992; Zhu & Anderson, 2002). The relevance of the setting considered is supported by the observation that non-negligible concentrations of dissolved *Cr(VI)* in groundwater bodies are documented in diverse geographical regions. For example, alarming concentrations of *Cr(VI)* are registered in Countries such as Italy, USA (California), Greece, Mexico, Japan and Indonesia, Brazil, Australia (e.g., Apollaro et al., 2011; Bourotte et al., 2009; Fantoni et al., 2002; Gray, 2003; Kaprara et al., 2015; Lelli et al., 2013; Mills et al., 2011; Morrill et al., 2013; Robles-Camacho & Armientac, 2000; Saputro et al., 2014; Kazakis et al., 2015, 2017). It is now well-established that the presence of *Cr(VI)* in natural waters can be linked to anthropogenic pollution and/or geogenic origins. Anthropogenic pollution stems from diverse manufacturing processes that can produce wastes containing chromium (e.g., Jacob & Testa, 2005; Kazakis et al., 2017; Vengosh et al., 2016). Relevant

concentrations of *Cr(VI)* are also found in natural waters for which anthropogenic causes are unlikely (e.g., Kaprara et al., 2015; Kazakis et al., 2015, 2017). In these cases, the origin of *Cr(VI)* can be traced to the progressive weathering due to interaction of ophiolitic and ultramafic outcrops and meteoric water. Note that an ophiolitic outcrop exposed to rain water may be partially or totally serpentinized even before getting in contact with meteoric water as a consequence of a different weathering process. According to Barnes and O'Neil (1978), the contact between ophiolitic outcrops and meteoric water at low temperature is however a feasible process that may lead to serpentinization and formation of lizardite/chrysotile minerals. Ophiolitic and ultramafic rocks are formed in igneous environments under very high temperature and pressure conditions and may contain a significant amount of chromium, mainly in the form of chromite ($FeCr_2O_4$; e.g., Ivarsson et al., 2011; Kazakis et al., 2015; Oze et al., 2004). When uplifted by geological processes and exposed to reduced temperature and oxygen and CO_2 partial pressures of shallow subsurface systems, these rocks progressively weather according to an irreversible kinetic process (Bethke, 2007; Styles et al., 2014). Depending on the composition of the parent igneous rock, the weathering process leads to the formation of a variety of secondary phases. When rainwater percolates through the rocks, its composition may be enriched by major, minor and trace elements released during weathering. After residing for some time within the weathering outcrops, the percolated water typically gushes out as a spring or feeds an alluvial aquifer (Kaprara et al., 2015; see Fig. 1 for a depiction of the hydrogeological setting considered). Several factors can control the chemical composition of the spring water, including, e.g., (*i*) the length of the flow path undertaken by the meteoric water in the subsurface, (*ii*) the associated residence time across the rock matrix system, (*iii*) the depth of the flow path relative to the ground surface, (*iv*) temperature and acidity conditions of the environment and, notably, (*v*) the redox conditions of the system and the mobility of the diverse ions released by the weathering process. Note that chromium is highly mobile in the hexavalent form while being characterized by a very limited solubility in its trivalent form, i.e., the valence state influences the

mobility of *Cr*, a feature observed for other commonly found chemical elements (e.g., *As*, *Fe*). Therefore, detectable amounts of chromium found in natural waters are typically in the form of the hazardous hexavalent form (Kaprara et al., 2015; Vengosh et al., 2016), while chromite-bearing rocks generally contain only the trivalent form (*Cr(III)*; Fantoni et al., 2002).

We perform sensitivity analyses according to three diverse sets of metrics and methodologies: (*i*) the Scatter Plots sensitivity analysis (SP, Saltelli et al., 2008); (*ii*) the Distributed Evaluation of Local Sensitivity Analysis (DELSA, Rakovec et al., 2014); and (*iii*) the moment-based global sensitivity analysis provided by Dell'Oca et al. (2017). We investigate the relative merits of the above illustrated set of approaches to sensitivity analyses of the target geochemical system. We also assess their ability to provide insights for geochemical model characterization and implementation, as well as for the optimization of the design of sampling campaigns, through the prioritization of the importance of model parameters according to multiple metrics. We do so by exploring and quantifying the sensitivity of the spring water speciation through a simplified geochemical model, i.e., upon relying on a reaction path modeling approach (Crawford, 1999; Zhu & Anderson, 2002). In this context, we analyze the impact of three input model parameters, i.e., (*i*) oxygen fugacity (f_{O2}), (*ii*) CO_2 fugacity (f_{CO2}), and (*iii*) temperature (*T*). These parameters are considered as proxies of the environmental conditions under which *Cr* oxidation takes place. Our choice to rest on a simplified geochemical model stems from the observation that a comprehensive mechanistic model of *Cr* dynamics would require considering both kinetic and equilibrium (bio)geochemical processes coupled to local flow and transport dynamics (McClain et al., 2017 and references therein). While considering such a modeling approach is fully compatible with our theoretical framework for uncertainty assessment, focusing on a setting associated with a limited number of uncertain parameters enables us to clearly illustrate and compare the salient points of the sensitivity analyses techniques we consider.

The physical process, the reaction chain, and the kinetics through which *Cr(III)* is oxidized to *Cr(VI)* have been largely discussed in the literature. According to thermodynamics arguments, spontaneous oxidation of *Cr(III)* is characterized by slow kinetics (Apte et al., 2005) and needs to be catalyzed to take place in a natural system at a significant rate. A variety of possible catalysts have been suggested to act to this end, including manganese oxides (Ivarsson et al., 2011; Kaprara et al., 2015; McClain et al., 2017), microbial activity (Fendorf et al., 2000; Ivarsson et al., 2011), hydrogen peroxide or simply free oxygen (Fantoni et al., 2002; Lin, 2002). While these processes are not explicitly included in our simplified approach, we treat oxygen fugacity as an effective indicator of the redox state of the system. As stated above, we remark that the framework of analysis is general and can be readily employed to analyze any geochemical model.

2 Conceptual model, uncertain parameters and focused outputs

2.1 Conceptual model

We summarize here a conceptual model of weathering of an outcrop of partially altered *Cr*-bearing ophiolites upon relying on the hydrogeological setting schematically depicted in Fig. 1 and illustrating the diverse water flow paths of meteoric water infiltrating into the subsurface.

The spring water composition is modeled upon taking into account the interaction between meteoric water and subsurface minerals. We consider the meteoric water chemical composition listed in Table 1. The latter has been derived through the procedure proposed by Boschetti and Toscani (2008) relying on the rain sample composition provided by Panettiere et al. (2000) and setting (*i*) CO_2 fugacity as log fCO_2 = -3.0; (*ii*) the temperature of the environment as 11 °C; (*iii*) a slight supersaturation of ferrihydrite-6 ($Fe(OH)_3$, with Saturation Index, *SI* = 0.00001) and kaolinite ($Al_2Si_2O_5(OH)_4$, with *SI* = 0.00001); and (*iv*) the value of the redox potential to be consistent with concentrations redox couple *N(-III)*/*N(V)*. To this end, we set concentrations of NH_4^+ and NO_3^- to 8.5×10^{-6} and 2.84×10^{-5} mol Kg^{-1},

149 respectively). Values listed in Table 1, given the low contents of sodium ($Na = 3.5 \times 10^{-5}$ mol Kg^{-1}) and
150 chlorine ($Cl = 3.9 \times 10^{-5}$ mol Kg^{-1}), can be considered as representative of precipitations across
151 continental regions. The assumed mineral composition is listed in Table 2. The most abundant phase is
152 *Al*-lizardite, an aluminum-enriched type of serpentine ($Mg_{2.7}Fe_{0.2}Al_{0.2}Si_{1.9}O_5(OH)_4$; Boschetti & Toscani,
153 2008). This scenario is typical of an ophiolitic outcrop showing an advanced state of serpentinization.
154 The source of chromium in the outcrop is constituted by a small amount of chromite (1%, in terms of
155 molar percentage, in our setting).

156 We model the spring water composition due to rock weathering upon relying on the reaction path
157 modeling in time-less mode. This approach was first proposed by Garrels and Mackenzie (1967),
158 formally implemented by Helgeson et al. (1969), and subsequently applied in several field studies (e.g.,
159 Censi et al., 2011; Marini, 2013; Taunton et al., 2010; Wood et al., 2006), and in hydrological scenarios
160 similar to the one considered in this work (see, e.g., Apollaro et al., 2011; Boschetti & Toscani, 2008;
161 Bruni et al., 2002; Fantoni et al., 2002; Helgeson, 1968; Helgeson et al.,1969, 1970; Lelli et al., 2013).
162 In this context, the evolution of an irreversible reaction towards its final equilibrium state can be
163 approximated by a sequence of partial equilibria (Marini, 2013). The term partial equilibrium indicates
164 that the dissolution of the ophiolitic rock across the weathering process is discretized into partial
165 equilibrium steps while the system is always in equilibrium with some selected mineral secondary phases.
166 The progress of the system is described in terms of the so-called progress variable ξ (that quantifies the
167 number of moles of ophiolitic rock forcedly dissolved) instead of time (Apollaro et al., 2011; Bruni et
168 al., 2002). This modeling approach is grounded on the experimental evidence that weathering is a very
169 slow and complex process: we assume that the limiting reaction process is the dissolution of primary
170 phases. The precipitation/dissolution of stable secondary phases is fast enough compared to dissolution
171 of primary phases to be modeled by thermodynamic equilibrium. Here, we assume that the secondary
172 mineral phases listed in Table 3 are allowed to precipitate as a consequence of ophiolites weathering.

The reaction path modeling is implemented in PHREEQC (Parkhurst & Appelo, 2013) with the LLNL database (Delany & Lundeen, 1991). The references used to extend the LLNL database are listed in Table 2 and Table 3. Additional details on the implementation of the reaction path modeling approach are illustrated in the Supplementary Material (Text S1).

We note that the employed geochemical model is associated with some important simplifications and embeds the following assumptions:

1. The rock is characterized by a spatially uniform composition and rainfall is the only source of recharge.

2. Spring water composition is expected to vary markedly as a consequence of environmental redox (*Eh*) and *pH* conditions. These factors are taken into consideration by introducing the dependence of the spring water composition on three parameters, i.e., the spring water temperature (*T*), the O_2 fugacity (f_{O2}), and the CO_2 fugacity (f_{CO2}), which are assumed to be constant, albeit affected by uncertainty.

3. We neglect the occurrence of catalytic processes and assume redox conditions to be driven by oxygen partial pressure, f_{O2}. As such, possible impacts of *Mn* oxides are neglected. We assume that the *Cr(III)* leached by chromite gives rise to *Cr(VI)* if the redox conditions (expressed in terms of *Eh*, as controlled by f_{O2} in our model) are compatible with the oxidized valence state of chromium (Apte et al., 2005; Fendorf, 1995). A similar assumption is considered for all redox species (even as this aspect is not always documented in natural systems, as seen by, e.g., Palandri & Reed, 2004 and references therein).

4. Coupling between geochemical and flow/transport processes is neglected. This implies that the subsurface system is modeled as a well-mixed reactor, the possible occurrence of incomplete

mixing and/or transport limitation of the reaction being disregarded. Temporal dynamics which could be associated with chemical reaction kinetics are also excluded. This is motivated by the observation that estimates of kinetic weathering reaction rate and fluid-mineral interfacial surface area can be uncertain or markedly hard to characterize due to paucity of data (Schott et al., 2012).

While being aware of the limitations offered by the geochemical model considered, we remark that our approach is (*a*) relatively straightforward to implement within available geochemical codes and (*b*) computationally inexpensive (i.e., a single model realization, corresponding to a given set of model parameters, runs in about 2s). Low computational costs give us the flexibility to fully explore sensitivity analyses and uncertainty propagation via numerical simulations (see also Section 4.2) with acceptable computational times and computer resources. The selected geochemical model still retains some information on typical environmental conditions characterizing settings where the weathering process takes place, and can provide some valuable preliminary indications on the system behavior in terms of model inputs that can be evaluated in a real scenario.

2.2 Uncertain model parameters and target outputs

We detail here the selected uncertain inputs and the implementation of the model illustrated in Section 2.1. We follow Neuman (2003a) and distinguish between modeling (Ye et al., 2005) and parametric uncertainties. Here, we explore the impact of the latter given the model structure introduced in Section 2.1.

We select f_{O2}, f_{CO2} and T as uncertain model parameters in agreement with previous studies (e.g., Boschetti & Toscani.,2008; Bruni et al., 2002; Fantoni et al., 2002; Lelli et al., 2013; Marini, 2013) and explore the way their uncertainty propagates to govern the variability of the spring water speciation. Fixing the fugacity of oxygen of the geochemical system is tantamount to controlling the environmental

redox condition, since *Eh* is directly related to f_{O2} for a given *pH* (Anderson, 2005). The fugacity of CO_2 is used as a controlling factor of the acidity of the environment (e.g., Bruni et al., 2002). Note that the variables f_{O2}, f_{CO2} and *T* can be interpreted as a proxy of the depth associated with the flowing path traveled by the meteoric water before being released to the spring. Low values of f_{O2} together with high values of f_{CO2} are representative of deep flowing paths across the fracture network, consistent with the observation that shallow hydraulic circuits can easily exchange mass with the external atmosphere where oxygen is abundant ($\log f_{O2} \approx -0.67$ and $\log f_{CO2} \approx -3.5$, f_{O2} and f_{CO2} being expressed in atm). Abundance of oxygen and CO_2 varies with depth depending on the efficiency of exchanges with the atmosphere (Bruni et al., 2002; Cipolli et al., 2004; Fantoni et al., 2002).

Our approach relies on the following steps (see Supplementary Material (Text S1, Fig. S1-S2) for more details):

1. We select the intervals of variation listed in Table 4 for the three uncertain inputs on the basis of literature analysis (Fantoni et al., 2002; Helgeson et al.,1969; Lelli et al., 2013). Note that we consider f_{O2} to vary between its value in free atmosphere and very low values that may be associated with deep water circuits. We label as Θ_1, Θ_2, and Θ_3 the intervals of variability of $\log f_{O2}$, $\log f_{CO2}$ and *T*, respectively.
2. We sample randomly the parameter space defined at Step 1 and generate a collection of PHREEQC input files (Step 3). Additional details on the sampling methods we employ depending on the considered sensitivity metric are illustrated in Section 3.
3. We simulate the weathering process using the reaction path modeling approach (see Section 2.1) for each generated parameter set. Advancement of the reaction modeling is discretized into 20 steps corresponding to the values of the progress variable ξ ranging from 5×10^{-9} mol to 1 mol. Target outputs (*Y*) of our analysis are the molalities of the following dissolved elements: *H+*, *C*, *Ca*, *Mg*, *Na*, *Fe*, *Cr(III)*, *Cr(VI)*, *Si*, *Al*, *Cl*, *N*, *S*, and *K*. The analysis of additional

outputs (e.g., alkalinity, amount of secondary phases, and/or ionic strength) that is potentially providing further insights on the problem under investigation can be considered as a future development.

3 Sensitivity analysis

Sensitivity analysis tools are briefly illustrated in the following Sections (SP in Section 3.1, DELSA in Section 3.2 and MM-GSA in Section 3.3). To simplify notation, we present the methods for three generic uncertain model parameters ϑ_1, ϑ_2 and ϑ_3. In our application these will correspond to log f_{O2}, log f_{CO2}, and T, respectively. The three-dimensional parameter support space is referred to as $\Omega = \Theta_1 \times \Theta_2 \times \Theta_3$.

3.1 Scatter Plots analysis (SP)

Scatter plots provide a qualitative sensitivity indication (Saltelli et al., 2008). We generate scatter plots through Monte Carlo sampling of the parameter space considering the three uncertain inputs as uniformly distributed independent random variables. We employ here $N = 10^5$ realizations of the model parameter set collected in vector $\mathbf{p}^{i,j,k} = \left(\vartheta_1^i, \vartheta_2^j, \vartheta_3^k\right)$ and obtain the corresponding outputs $Y^{i,j,k}$ through the geochemical model described in Section 2.2. Given the N samples of $\mathbf{p}^{i,j,k}$ and the corresponding values of $Y^{i,j,k}$, scatter plots are obtained by plotting the N values of the selected output $Y^{i,j,k}$ against the N values of each of the input factors (i.e., ϑ_1^i, ϑ_2^j, ϑ_3^k**)**. Scatter plots can be informative to assess trends of output variations as a function of a single parameter. Otherwise, they can hardly be used as a stand-alone tool, as they do not provide a synthetic appraisal of sensitivity. Exploring the scatter plots associated with each of the 20 steps of the progress variable ξ requires constructing a large amount of graphs whose analysis may become cumbersome (i.e., in our case this would imply constructing 840

plots for the analysis of the impact of 3 input factors on 14 model outputs selected at each of the 20 progress variable steps).

3.2 Distributed Evaluation of Local Sensitivity Analysis (DELSA)

Local sensitivity analysis methods are typically based on the computation of local derivatives of the model output *Y* with respect to parameter values corresponding to a specific location in the parameter space. The information about relative parameter importance is limited to the single location where the local derivative is assessed and these results can be extended to the entire parameter space only if the model displays a linear behavior with respect to input parameters. To reveal how the sensitivity of a model output varies across the parameter space, Rakovec et al. (2014) suggest performing a Distributed Evaluation of Local Sensitivity Analysis (DELSA). The latter essentially consists of performing multiple evaluations of a local sensitivity metric across the parameter space. We list here for convenience the main points of the steps required to conduct DELSA (see Rakovec et al., 2014 for additional details):

1. We sample the parameter space along each dimension with constant spacing Δ_h (with h = 1, 2, 3, respectively for Θ_1, Θ_2 and Θ_3). This yields a set of $M = m_1 \cdot m_2 \cdot m_3$ sampling points $\mathbf{p}^{i,j,k}$, where m_h represents the number of sampling points along each coordinate in the parameter space. We then evaluate the model output $Y^{i,j,k}$ for each sampling point.
2. We approximate the local derivatives with respect to ϑ_1 at a given evaluation point $\mathbf{p}^{i,j,k}$ as

$$\left.\frac{\partial Y}{\partial \vartheta_1}\right|_{\mathbf{p}^{i,j,k}} \approx \frac{Y(\vartheta_1^{i+1}, \vartheta_2^j, \vartheta_3^k) - Y(\vartheta_1^i, \vartheta_2^j, \vartheta_3^k)}{\Delta_1} \qquad i = 1,\ldots m_1 - 1 \tag{1}$$

We compute the local derivatives with respect to ϑ_2 and ϑ_3 as in (1).

3. We compute the local variance of the target output $V_L^{i,j,k}$ associated with each location $\mathbf{p}^{i,j,k}$ as

$$V_L^{i,j,k} = \left(\left.\frac{\partial Y}{\partial \vartheta_1}\right|_{\mathbf{p}^{i,j,k}}\right)^2 s_1^2 + \left(\left.\frac{\partial Y}{\partial \vartheta_2}\right|_{\mathbf{p}^{i,j,k}}\right)^2 s_2^2 + \left(\left.\frac{\partial Y}{\partial \vartheta_3}\right|_{\mathbf{p}^{i,j,k}}\right)^2 s_3^2 \tag{2}$$

where $s_j^2 = \sigma^2(\vartheta_j)$ is the *a priori* variance of ϑ_j. Equation (2) represents the local variance of the target output under the following assumptions: (*i*) the random input factors are characterized by uniform distributions and (*ii*) the variance computation relies only on *a priori* information about the parameters (Rakovec et al., 2014).

4. The local sensitivity indices are then defined as (see Rakovec et al., 2014)

$$SL_1^{i,j,k} = \frac{\left(\left.\frac{\partial Y}{\partial \vartheta_1}\right|_{\mathbf{p}^{i,j,k}}\right)^2 s_1^2}{V_L^{i,j,k}}; \quad SL_2^{i,j,k} = \frac{\left(\left.\frac{\partial Y}{\partial \vartheta_2}\right|_{\mathbf{p}^{i,j,k}}\right)^2 s_2^2}{V_L^{i,j,k}}; \quad SL_3^{i,j,k} = \frac{\left(\left.\frac{\partial Y}{\partial \vartheta_3}\right|_{\mathbf{p}^{i,j,k}}\right)^2 s_3^2}{V_L^{i,j,k}} \tag{3}$$

The four-steps procedure here presented is repeated $(m_1 - 1)(m_2 - 1)(m_3 - 1)$ times to estimate the distribution of the local indices defined in (3) throughout the parameter space. Hereafter, distributions of $SL_1^{i,j,k}$, $SL_2^{i,j,k}$ and $SL_3^{i,j,k}$ in the parameter space are denoted as *sensitivity maps* of ϑ_1, ϑ_2, and ϑ_3, respectively. To avoid artificially high values of local indices due to numerical issues associated with low local variance values, we estimate the local coefficient of variation ($LCV_h^{i,j,k}$)

$$LCV_h^{i,j,k} = \frac{\sqrt{V_L^{i,j,k}}}{Y^{i,j,k}}; \qquad h = 1, 2, 3 \tag{4}$$

and force index $SL_h^{i,j,k}$ to zero at all locations $\mathbf{p}^{i,j,k}$ where $LCV_h^{i,j,k} < 1 \times 10^{-2}$. A refined grid in the parameter space has also been analyzed to assess the stability of the results presented in this study and no significant differences have been observed (details not shown).

One should note that (*i*) the implementation of DELSA is generally less computationally intensive than several global sensitivity analysis tools (e.g., Sobol' statistics) and (*ii*) allows exploring *factor mapping* (according to the terminology of Saltelli et al., 2008) or *regions of sensitivity* identification (according to the terminology of Razavi & Gupta, 2015). The latter relies on dividing the parameter space in sub-regions where the model output sensitivity shows a diverse behavior in response to the same variation of a random input.

A somehow limiting aspect of DELSA is the large amount of *sensitivity maps* that can be obtained as result of the method implementation. In our study we obtain three *sensitivity maps* (one for each input parameter) for each model output *Y* investigated for each step ξ. Considering all of the outputs subject to our investigation and the number of ξ steps simulated, this yields a total of 840 *sensitivity maps*.

Where sensitivity to a parameter of interest, e.g., ϑ_1, is identified, one can introduce the following indicator

$$\langle SL_1 \rangle^i = \frac{\sum_{j=1}^{m_2-1} \sum_{k=1}^{m_3-1} SL_1^{i,j,k}}{(m_3-1)(m_2-1)} \tag{5}$$

The latter corresponds to averaging SL_1 along directions ϑ_2 and ϑ_3 and yields the quantity $\langle SL_1 \rangle^i$ that is only a function of ϑ_1 and the reaction progress variable step ξ; quantity $\langle SL_1 \rangle^i$ can then be complemented by its standard deviation, defined as

$$STD^i = \sqrt{\frac{\sum_{j=1}^{m_2-1} \sum_{k=1}^{m_3-1} \left(SL_1^{i,j,k} - \langle SL_1 \rangle^i \right)^2}{(m_2-1)(m_3-1)}} \tag{6}$$

3.3 Moment-based Metrics for Global Sensitivity Analysis (MM-GSA)

The global sensitivity metrics suggested by Dell'Oca et al. (2017) are here implemented to quantify the impact of the input factor uncertainties on statistical moments driving key features of the structure of the probability density function (*pdf*) of model outputs. These authors propose estimating sensitivity indices based on the first four (statistical) moments of the *pdf* of a model output (i.e., mean, variance, skewness and kurtosis). Here, we confine our analysis to the mean and variance and employ the metrics

$$AMAE_{\vartheta_j} = \begin{cases} \frac{1}{|Y_0|} E\left[\left|Y_0 - E[Y|\vartheta_j]\right|\right] & if \quad Y_0 \neq 0 \\ E\left[\left|E[Y|\vartheta_j]\right|\right] & if \quad Y_0 = 0 \end{cases} \tag{7}$$

$$AMAV_{\vartheta_j} = \frac{E\left[\left|V[Y] - V[Y|\vartheta_j]\right|\right]}{V[Y]} \tag{8}$$

where $AMAE_{\vartheta_j}$ and $AMAV_{\vartheta_j}$ respectively represent the sensitivity indices associated with the first and the second moment of the target model output *Y*; quantity Y_0 in (7) indicates the (unconditional) mean of *Y*, i.e., the mean value computed over the entire parameter space; the symbols $E[\bullet]$ and $V[\bullet]$ respectively identify expected value (i.e., the mean) and variance; the symbol $Y|\vartheta_j$ indicates conditioning of *Y* to a known value of parameter ϑ_j. Essentially, indices $AMAE_{\vartheta_j}$ and $AMAV_{\vartheta_j}$ quantify the expected change of the mean and variance of *Y* due to our knowledge of (or conditioning on) ϑ_j. Large values of these indices indicate that the variability of the input markedly affects the considered moments of the output *pdf*. We estimate these indices by way of the same Monte Carlo sample used for the scatter plot analysis. Conditional statistics are evaluated upon subdividing the sample in classes (e.g., Saltelli et al., 2008).

To avoid artificially high values of $AMAV_{\vartheta_j}$ occurring when the variance $V[Y]$ is very small, we introduce

$$CV = \frac{\sqrt{V[Y]}}{Y_0} \tag{9}$$

and force to zero the index value if $CV < 1 \times 10^{-2}$.

A strength of the MM-GSA approach is to condense the impact of random input factors on a moment of the *pdf* of each target model output through a limited number of indices, thus streamlining the elaboration and interpretation of the results. Otherwise, information on local sensitivity is shadowed. The MM-GSA method proposed by Dell'Oca et al. (2017) is more informative than other commonly

used GSA variance based methods (such as, e.g., the Sobol' indices based on the classical decomposition of variance) because it considers the way the moments driving structure of the *pdf* of the target output are affected by the uncertainty associated with each model parameter. A limitation of the MM-GSA is that a large number of Monte Carlo model realizations might be required in some cases to obtain a robust and stable estimation of the moment-based metrics. This barrier could be in some instances alleviated by resorting to the use of surrogate (or reduced-order) models (Dell'Oca et al., 2017). Here, we verify that a number of model runs $N = 10^5$ was sufficient to attain stability of the MM-GSA indices computed.

4 Results

We focus on a selection of the results obtained with the sensitivity analysis tools introduced in Section 3. Results are illustrated for three exemplary reaction steps, i.e., $\xi_1 = 1 \times 10^{-8}$ mol, $\xi_2 = 1 \times 10^{-4}$ mol and $\xi_3 = 0.5$ mol. This Section is structured in two parts: in Section 4.1 we discuss the results associated with the identification of regions of sensitivity, i.e., the analysis of the SPs and the implementation of DELSA; Section 4.2 is devoted to the discussion of the results of MM-GSA. Results presented here focus on selected outputs (*Cr* speciation, *C* molality and *pH*) and are complemented by those given in the Supplementary Material (Text S2 and Figures S3-S5) for other chemical species (*Si*, *Fe*, *Ca*).

4.1 Local sensitivity analysis across the parameter space and regions of sensitivity

In this Section we analyze trends and features displayed by key outputs as a function of the three uncertain model parameters, through visualization of results encapsulated in SPs (Fig. 2) and DELSA (Fig. 3-5). These analyses are performed following the procedures described in Section 3. We employ $N = 10^5$ realizations for SPs and $\Delta_1 = 2$, $\Delta_2 = 0.2$, and $\Delta_3 = 1$ as discretization steps for DELSA (leading to $M = 1188$ realizations).

4.1.1 Chromium speciation

Values of *Cr(VI)* molality vary with ξ, remarkably similar qualitative patterns of the data clouds being observed as a function of $\log f_{O2}$ for the diverse ξ levels considered (see Fig. 2a). We note that the molality of *Cr(VI)* steadily decreases for decreasing values of $\log f_{O2}$ (for $\log f_{O2} < -20$). When $-42 \le \log f_{O2} \le -30$, the amount of dissolved *Cr(VI)* is smaller than 10^{-6}, 10^{-8}, and 10^{-14} mol kg^{-1}, respectively at ξ_1, ξ_2, and ξ_3, i.e., it is lower than 0.5% of the total chromium in the system at each step and lies below the field detection limit (Ball & Izbickib, 2004) for $-42 \le \log f_{O2} \le -35$. Molality of *Cr(VI)* is constant across all realizations for $\log f_{O2} > -20$ and for each of the three considered values of ξ coincides with the total amount of chromium released by the weathering of ophiolitic rock, i.e., the total amount of chromium present in the system. This result is a consequence of the high solubility of *Cr(VI)* in water (Fendorf, 1995). Otherwise, *Cr(III)* is present in negligible amounts in water for $\log f_{O2} > -20$ (see also Bai & Fan, 2009) and we verify that it never exceeds the detection limit in this range of values of $\log f_{O2}$ across all Monte Carlo realizations. Scatter plots of *Cr(III)* versus $\log f_{O2}$ display trends mirroring those of *Cr(VI)* in Fig. 2a (not shown). Figs. 2b and c depict the scatter plots for *Cr(VI)* as a function of $\log f_{CO2}$ and *T*. These results suggest a linear dependence (on average) of the molality of *Cr(VI)* on both $\log f_{CO2}$ (Fig. 2b) and *T* (Fig. 2c) and indicates a mild sensitivity of *Cr(VI)* with respect to these two factors. A similar behavior is also observed for *Cr(III)* (not shown).

Fig. 3 depicts $\left\langle SL_{f_{O2}} \right\rangle^i$ as function of $\log f_{O2}$ and the reaction progress variable ξ computed for the *Cr* molality apportioned in its two forms, i.e., *Cr(VI)* (Fig. 3a) and *Cr(III)* (Fig. 3b). These results clearly suggest the presence of three *regions of sensitivity* for any ξ: (*i*) for $-42 < \log f_{O2} < -30$ the local sensitivity of the molality of *Cr(VI)* is completely controlled by oxygen fugacity, molality of *Cr(III)* being only slightly sensitive to $\log f_{O2}$; (*ii*) for $-30 < \log f_{O2} < -20$, molalities of *Cr(VI)* and *Cr(III)* are

386 both sensitive to $\log f_{O2}$ revealing a pattern according to which a large $\left\langle SL_{f_{O2}} \right\rangle^i$ value for *Cr(VI)*

387 corresponds to a small value for *Cr(III)* at a fixed $\log f_{O2}$; and (*iii*) for $-20 < \log f_{O2} < -0.67$ the local

388 sensitivity of *Cr(III)* molality is fully controlled by oxygen fugacity, while the molality of *Cr(VI)* is not

389 sensitive to $\log f_{O2}$. These results suggest that these two forms of chromium can coexist in water in

390 detectable amounts solely for the limited range $-30 \leq \log f_{O2} \leq -20$ (corresponding to the conditions

391 characterizing the transition from shallow groundwater to deeper hydraulic circuits leading to more

392 evolved *Ca*-enriched waters; see also Fantoni et al., 2002; Lelli et al., 2013) and the relative proportions

393 of *Cr(III)* and *Cr(VI)* within this region is sensitive to $\log f_{O2}$. Otherwise, the role of $\log f_{O2}$ is no longer

394 relevant for the chromium valence state partitioning for $-20 \leq \log f_{O2} \leq -0.67$ (a setting ascribed to

395 shallow groundwater circulation leading to *Mg-HCO3* rich waters; see also Fantoni et al., 2002; Lelli et

396 al., 2013) and the total amount of chromium is found in the form of *Cr(VI)*.

397 4.1.2 *pH* and Carbon speciation

398 Fig. 2d depicts the scatter plot of *pH* as a function of log f_{O2} at $\xi_1 = 1\times10^{-8}$ mol (black circles),

399 $\xi_2 = 1\times10^{-4}$ mol (red circles) and $\xi_3 = 0.5$ mol (blue circles). Results obtained for $\xi_1 = 1\times10^{-8}$ mol

400 suggest that *pH* is not sensitive to $\log f_{O2}$ for $-42 \leq \log f_{O2} \leq -10$ and $-5 \leq \log f_{O2} \leq -0.67$. The *pH*

401 values sharply decrease with increasing log f_{O2} for $-10 \leq \log f_{O2} \leq -5$. This behavior is associated with

402 nitrogen speciation in water which, in turn, is affected by f_{O2} (i.e., by the redox state). For small values

403 of ξ, nitrogen, sulfur and chloride are abundant, as compared against other elements, given the

404 composition of the meteoric water (see Table 1). In the range of oxygen partial pressure explored in our

405 simulations, the nitrogen may appear in two different stable valence states: (*i*) *N(0)* is the dominant

406 valence state of nitrogen for $-42 \leq \log f_{O2} \leq -10$, with negligible content of *N(V)* in the water; (*ii*)

407 nitrogen is present solely as *N(V)* for $-5 \leq \log f_{O2} \leq -0.67$. Detectable amounts of *N(0)* and *N(V)* coexist

in solution within the interval $-10 \le \log f_{O2} \le -5$ (not shown). These features have a definite impact on *pH*, as the oxidized *N(V)* form of nitrogen is prone to generating acid compounds in water, such as HNO_3^-, which favors the decrease of *pH* of the solution. Otherwise, the formation of the neutral compound N_2 is favored when the *N(0)* reduced form dominates. Therefore, *pH* is higher for $-42 \le \log f_{O2} \le -10$ (i.e., when nitrogen is reduced to *N(0)*) than for $-5 \le \log f_{O2} \le -0.67$ (i.e., when nitrogen is oxidized to *N(V)*). In the range $-10 \le \log f_{O2} \le -5$, *pH* responds proportionally to the relative abundancy of the *N(V)* and *N(0)* in which nitrogen is apportioned. Values of *pH* are then seen to decrease as log f_{O2} increases, consistent with the increase of *N(V)* at the expenses of *N(0)*.

For $\xi = 0.5$ mol, a slight and localized variation of *pH* is observed (blue circles in Fig. 2d) in the interval $-30 \le \log f_{O2} \le -20$, while *pH* appears to be insensitive to $\log f_{O2}$ for $-42 \le \log f_{O2} \le -30$ and $-20 \le \log f_{O2} \le -0.67$. For $-30 \le \log f_{O2} \le -20$, *pH* varies in response to the transition of dissolved chromium discussed in Section 4.1.1. Similar to the case of nitrogen, dissolved *Cr(VI)* is found in chromic acid (H_2CrO_4), which is partially or totally dissociated into $HCrO_4^-$ and CrO_4^{2-} and may acidify the water solution. Otherwise, *Cr(III)* is chemically affine to the hydroxyl group (OH^-) leading to the formation of $Cr(OH)_2^+$, $Cr(OH)^{2+}$ and Cr^{3+}, which can buffer the acidity of the solution (Motzer & Engineers, 2004).

We observe negligible sensitivity of *pH* to f_{O2} for $\xi = 1\times10^{-4}$ mol (red circles in Fig. 2d). This behavior is likely related to the observation that the progressive alteration of the ophiolitic rock has an alkalizing effect on the pore water, as reported by Oze et al. (2004) and evidenced in Fig. 2d by the overall increment of *pH* as reaction advances. It can also be observed that, irrespective of the increase of *pH* with ξ, the alkalinity is not strong enough to entirely buffer the *pH* alteration ascribed to large amounts of chromate ion formed at large ξ for $-20 \le \log f_{O2} \le -0.67$. Fig. 2e-f show that *pH* tends to

429 decrease as $\log f_{CO2}$ increases, independent of ξ (Fig. 2e), while temperature has a negligible overall
430 impact on the *pH* of the final solution.

431 Fig. 4 depicts six *sensitivity maps* resulting from the DELSA and targeting *pH* as a model output.
432 Fig. 4a, b, and c respectively depicts the *sensitivity maps* of $SL_{f_{O2}}$, $SL_{f_{CO2}}$ and SL_T evaluated at $\xi = 0.5$
433 mol. Corresponding depictions for $\xi = 1\times10^{-8}$ mol are included in Fig. 4d, e, and f. These maps show that
434 the *pH* of the solution is chiefly influenced by $\log f_{CO2}$ for most of the parameter combinations within
435 the selected parameter space. Notable exceptions are given by localized regions where the effect of
436 $\log f_{O2}$ becomes prevalent, i.e., for $-30 \le \log f_{O2} \le -20$ (Fig. 4a) when $\xi = 0.5$ mol and for
437 $-10 \le \log f_{O2} \le -5$ when $\xi = 1\times10^{-8}$ mol (Fig. 4d). This behavior is consistent with our comments above
438 related to the sensitivity to $\log f_{O2}$ of the apportionment between the redox couples *N(0)/N(V)* and
439 *Cr(III)/Cr(VI)*.

440 The dependence of the extent of the sensitivity regions of *pH* on $\log f_{O2}$ and ξ can be clearly
441 visualized upon considering $\left\langle SL_{f_{O2}} \right\rangle^i$ (Fig. 5a). Note that shaded areas highlighted in the plane ($\log f_{O2}$,
442 ξ) in Fig. 5 correspond to the ranges of $\log f_{O2}$ values associated with the transition of the dominant
443 valence state of *Cr* (yellow area) and *N* (red area). The pattern of $\left\langle SL_{f_{O2}} \right\rangle^i$ computed for the molality of
444 H^+ at $\xi = 1\times10^{-8}$ mol is very similar to the one observed at all reaction progress steps 1×10^{-8} mol $\le \xi \le$
445 1×10^{-4} mol. For 1×10^{-4} mol $< \xi \le 1\times10^{-1}$ mol, $\left\langle SL_{f_{O2}} \right\rangle^i$ vanishes throughout Θ_1. This is consistent with
446 the results depicted in the scatter plots of *pH* versus log *f*$_{O2}$ for $\xi = 1\times10^{-4}$ mol (red circles in Fig. 2d).
447 Then, for the interval ξ = [1×10^{-4} mol, 1×10^{-1} mol] the increase of solution alkalinity (resulting from
448 ophiolitic rock alteration) completely buffers the release of H^+ resulting from oxidized chromium as well
449 as nitrogen valence states. Nonzero values of sensitivity to $\log f_{O2}$ are found for $\xi > 1\times10^{-1}$ mol, (i.e.,

for advanced stages of the reaction) solely across the shaded yellow area in Fig. 5a. Sensitivity of H^+ to $\log f_{O2}$ generally increases as ξ increases from 1×10^{-1} to 1. This behavior is a consequence of the larger amount of chromium released by the altered rock in the solution, which, in turn, markedly alters *pH* when the oxidizing conditions favor speciation to *Cr(VI)* at the expenses of *Cr(III)*.

Fig. 5b depicts the evolution of $\left\langle SL_{f_{O2}} \right\rangle^i$ associated with dissolved carbon as a function of $\log f_{O2}$ and ξ. Carbon speciation in water is heavily influenced by *pH* and the trends observed in Fig. 5b naturally follow those in Fig. 5a. A remarkable difference between these two trends is observed for $1\times10^{-4} \leq \xi \leq 1\times10^{-2}$, where the dissolved carbon shows a mild sensitivity to $\log f_{O2}$ (note the nonzero values of $\left\langle SL_{f_{O2}} \right\rangle^i$) across the two colored shaded areas in Fig. 5b. These results are consistent with the observation that the alkalinity (to which the ion HCO_3^- contributes) of the solution is sufficient to maintain the *pH* stable at these reaction stages even as the change of the valence state of *Cr* and *N* may release H^+ ions. The significance and implications of this finding might be further explored upon considering the dynamics of the assumed secondary phases, an analysis that is beyond the scope of this study.

4.1.3 Identification of sensitivity regions

The *sensitivity maps* obtained from DELSA together with the SPs analysis show that the variability of $\log f_{O2}$ has a pivotal role to sensitivity of many model outputs, i.e., H^+, *C*, *Ca*, *Mg*, *Na*, *Fe*, *Cr(III)*, *Cr(VI)*, *Al*, and *K*. This result is not surprising given that the system under consideration is driven by redox state. In this context, our analysis documents that the importance of oxygen fugacity is not uniform across the parameter space. One can easily identify two sub-regions of Θ_1 where the variability of $\log f_{O2}$ may be considered the only element contributing to the target output variances. Sensitivity of

target variables to $\log f_{O2}$ vanishes in the remaining regions of Θ_1, where it is driven solely by $\log f_{CO2}$ and *T*.

We can then identify the following *regions of sensitivity* associated with the model presented in this work by relying on the results of Figs. 2-5 and partitioning Θ_1 onto five intervals I_w (w = 1, 2, 3, 4, 5):

1. $\{I_1 : \log f_{O2} \in [-42,-30]$, $\log_{f_{CO2}} \in \Theta_2$, and $T \in \Theta_3\}$: all model outputs are insensitive to $\log f_{O2}$ in this interval across the range of ξ explored; an exception is given by the molality of *Cr(VI)* that is very sensitive to $\log f_{O2}$, a feature which is not of practical interest because of the negligible amount of *Cr(VI)* in the solution.
2. $\{I_2 : \log f_{O2} \in [-30,-20]$, $\log_{f_{CO2}} \in \Theta_2$, and $T \in \Theta_3\}$: several model outputs (H^+, *Ca*, *C*, *Fe*, *Mg*, *K*, *Na*, *Al*) are sensitive to $\log f_{O2}$ in this interval only for large values of the progress variable ξ. This result can be interpreted as an indirect consequence of the change of proportion between *Cr(III)* and *Cr(VI)* as a function of $\log f_{O2}$. Outside of I_2, only one valence state of chromium is detectable in the spring water for large values of ξ.
3. $\{I_3 : \log f_{O2} \in [-20,-10]$, $\log_{f_{CO2}} \in \Theta_2$, and $T \in \Theta_3\}$: all model outputs are not sensitive to $\log f_{O2}$ in this interval across the range of ξ explored; an exception is given by the molality of *Cr(III)* that is very sensitive to $\log f_{O2}$ but otherwise associated with negligible values in the system.
4. $\{I_4 : \log f_{O2} \in [-10,-5]$, $\log_{f_{CO2}} \in \Theta_2$, and $T \in \Theta_3\}$: some model outputs (H^+, *C*, *Al*) are sensitive to ϑ_1 in this interval, with a high level of sensitivity registered only for small values of the progress variable ξ. From a physical point of view, this results can be seen as an indirect consequence of the change of proportion between *N(0)* and *N(V)* as a function of log f_{O2}. Outside

493 of I_4, only one valence state of chromium is detectable in the spring water for small ξ. Note that
494 the amount of *Cr(III)* is still negligible within I_4, similar to what observed for I_3.

495 5. $\{I_5 : \log f_{O2} \in [-5, -0.67],\ \log_{f_{CO2}} \in \Theta_2$, and $T \in \Theta_3\}$: all model outputs are insensitive to f_{O2} in
496 this interval across the range of ξ explored. The molality of *Cr(III)* stands as an exception also
497 in this region and, similar to I_4 and I_3, the interest of this target variable in this interval is negligible
498 due to the very low quantity of *Cr(III)* that can be found in water.

499 **4.2 Global Sensitivity Analysis**

500 The analysis illustrated in Section 4.1 suggests that a set of distinct *regions of sensitivity* can be
501 demarcated in the parameter space. Here, we compare MM-GSA indices $AMAE_j$ and $AMAV_j$ (here, *j*
502 stands for f_{O2}, f_{CO2}, or *T*) computed considering the full parameter space Ω against their counterparts
503 evaluated within each of the partitions I_w (w = 1, 2, ..., 5) defined in Section 4.1.3. In the following, we
504 term the latter as region-specific sensitivity indices.

505 Fig. 6 depicts the results obtained by the computation of the MM-GSA indices $AMAE_j(\Omega)$ and
506 $AMAE_j(I_w)$ (filled circles) for H^+. Global sensitivity measures generally indicate that CO_2 fugacity has
507 the largest influence on H^+, followed by oxygen fugacity and temperature, for $\xi = 1\times10^{-8}$, and 0.5 mol.
508 For $\xi = 1\times10^{-4}$ mol, H^+ is exclusively sensitive to $\log f_{CO2}$ and displays negligible sensitivity to
509 temperature and oxygen fugacity. Large discrepancies are observed between $AMAE_{f_{O2}}(\Omega)$ and
510 $AMAE_{f_{O2}}(I_w)$ for $\xi = 1\times10^{-8}$ and 0.5 mol. Region-specific sensitivity indices $AMAE_{f_{O2}}(I_w)$ indicate that
511 oxygen fugacity influences H^+ only within intervals I_4 (for $\xi = 1\times10^{-8}$ mol) and I_2 (for $\xi = 0.5$ mol)
512 (Fig. 6a-c, blue filled circles). Note that $AMAE_{f_{O2}}(I_2) = 0.11$ for $\xi = 0.5$ mol, while $AMAE_{f_{O2}}(I_4) = 0.54$
513 for $\xi = 1\times10^{-8}$ mol indicating a larger sensitivity for H^+ in I_4 than in I_2. This result is in agreement with

514 our conclusions inferred from the scatter plots presented in Section 4.1 (Fig. 2d) and provides a
515 quantification of the qualitative behavior evidenced by the SPs. Indices $AMAE_{f_{CO2}}(I_w)$ (red filled circles,
516 Fig. 6a-c show that CO_2 fugacity is the most important controlling factor for the mean of H^+ across the
517 bulk of the parameter space, the only exception being given by interval I_4 for $\xi = 1\times10^{-8}$ mol (Fig. 6a,
518 where $AMAE_{f_{O2}}(I_4) > AMAE_{f_{CO2}}(I_4)$). Sensitivity to temperature T does not show significant variations
519 for the three investigated values of ξ, both global and region-specific indices associated with it never
520 exceeding a value of 0.1. Temperature would be ranked as the least influential parameter on the basis of
521 global sensitivity indices computed upon considering the entire parameter space Ω. However, it can also
522 be observed that H^+ is more sensitive to temperature than to f_{O2} across the parameter space with the
523 exception of intervals I_4 (for $\xi = 1\times10^{-8}$ mol) and I_2 (for $\xi = 0.5$ mol), as discussed above. The
524 qualitative trend of $AMAE_j(I_w)$ is analogous to the one of $AMAV_j(I_w)$, shown in Fig. 6d-f. We can then
525 infer that the sample mean and variance of H^+ are characterized by similar sensitivities to the selected
526 input factors.

527 Results in Fig. 6 reveal possible limitations associated with global sensitivity measures. As an
528 example, Fig. 6a shows that $AMAE_{f_{O2}}(\Omega) = 0.28$, $AMAE_{f_{CO2}}(\Omega) = 0.42$, and $AMAE_T(\Omega) = 0.03$, i.e.
529 that the sample mean of the output is chiefly influenced by $\log f_{CO2}$ (related to alkalinity), followed by
530 $\log f_{O2}$ (related to redox conditions), while T has a negligible influence on H^+. This behavior is mainly
531 driven by the large sensitivity to $\log f_{O2}$, which is actually confined to region I_4 but yields high values
532 of $AMAE_{f_{O2}}(\Omega)$. This shows that effects of locally high sensitivities can be propagated to global
533 measures relying on the entire sampling domain Ω. Note that the global nature of $AMAE_{f_{O2}}(\Omega)$ masks
534 the richness of information related to the distribution of the sensitivity across the parameter space. In
535 other words, relying on an index such as $AMAE_{f_{O2}}(\Omega)$ prevents distinguishing between cases in which

536 the sensitivity to the random input factor is high and uniformly distributed across Ω (see, e.g., the
537 sensitivity to $\log f_{CO2}$ in Fig. 6b) from cases where only isolated high sensitivity peaks occur (see, e.g.,
538 the sensitivity to $\log f_{O2}$ in Fig. 6a).

539 Similar considerations can be made by comparing indices $AMAE_j(I_w)$ and $AMAE_j(\Omega)$ (or
540 equivalently $AMAV_j$) for all of the other outputs displaying a local variation of parameter sensitivity
541 according to DELSA and SPs analysis. Fig. 7 depicts the results of the MM-GSA metrics evaluated for
542 *Cr(III)* (Fig. 7a, c) and *Cr(VI)* (Fig. 7b, d) at ξ = 0.5. Parameter ranking remarkably varies also in these
543 cases when considering the global and region-specific indices. We observe (Fig. 7a, c) the occurrence of
544 quite large values for $AMAE_{f_{O2}}(I_w)$ and $AMAE_{f_{CO2}}(I_w)$ in I_2, I_3, I_4, and I_5 for *Cr(III)*, values associated
545 with *Cr(VI)* being largest in I_1 and I_2.

546 # 5 Conclusions

547 Our work leads to the following major conclusions.

548 1. Our study suggests that SPs, DELSA and MM-GSA lead to coherent results and
549 complementary information when properly implemented and interpreted and highlights the
550 importance of combining diverse sensitivity measures in geochemical modeling. Scatter plots
551 and DELSA provide quantitative and qualitative criteria to demarcate localized *regions of*
552 *sensitivity* in the parameter space, which may arise for localized changes in the chemistry of
553 the solution. In the case of *Cr* oxidation, alteration of redox couples' equilibrium induces
554 localized changes in the model responses, which in turn yield regionalized sensitivity
555 responses.

556 2. We delineate five *regions of sensitivity* based on the influence of the oxygen partial pressure
557 on the model outputs. The importance of f_{O2} is inhomogeneous across the parameter space and

this parameter induces nonlinear variations in the output, driven by shifts in the redox couples concentrations. Analysis of SPs enables us to associate the variation of local model sensitivity across the parameter space with the valence state transition of *N(0)* into *N(V)* and *Cr(VI)* into *Cr(III)*, and *vice versa*. The reduced form of nitrogen tends not to impact on the solution *pH*, while the reduced form of chromium typically induces an increase in *pH*. The oxidized form of both of these elements are associated with acid solutions. With an increase of nitrogen or chromium molality, *pH* varies according to the water redox conditions and the sensitivity of nitrogen and chromium valence state to the redox conditions is propagated through *pH* to the entire spring water speciation (i.e., *Ca*, *Mg*, *K*, *Al*, *Na*, *Fe* molalities).

3. In settings where the model response displays a regionalized sensitivity output of the kind illustrated above, MM-GSA indices largely depend on the selection of the parameter space. For example, the sensitivity of the mean *pH* to oxygen fugacity becomes predominant over temperature and carbon dioxide fugacity within well-defined regions of the wide parameter space explored. The combination of local and global sensitivity measures is then key to understand the relationship between global and region-specific parameter ranking. This conclusion is markedly relevant when sensitivity measures are employed to drive and design experimental measurements campaigns.

The identified *regions of sensitivity* and the model outputs sensitivities observed are specifically associated with the simplified geochemical model of *Cr* oxidation and leakage investigated here. Otherwise, the procedure implemented can be readily extended to any other natural geochemical model relying on a diverse physical system and conceptual outline. As redox- sensitive (e.g., *Fe*, *N*, *S*, *Cl*, *Cr*, *As*) elements are ubiquitous in natural systems, we envision our results to be relevant to a large class of environmental problems.

6 Acknowledgments

The authors would like to thank the EU and MIUR for funding, in the frame of the collaborative international Consortium (WE-NEED) financed under the ERA-NET WaterWorks2014 Cofunded Call. This ERA-NET is an integral part of the 2015 Joint Activities developed by the Water Challenges for a Changing World Joint Programme Initiative (Water JPI).

Data to generate the results are available at the following link: https://data.mendeley.com/datasets/57pk2fwwsn/draft?a=3301ed25-5a7f-4e0e-a5a8-9a5baeceba58.

REFERENCES

Anderson, G. M. (2005). *Thermodynamics of natural systems*, Cambridge, UK: Cambridge University Press.

Apollaro, C., Marini, L., Critelli, T., Barca, D., Bloise, A., De Rosa, R et al. (2011). Investigation of rock-to-water release and fate of major, minor, and trace elements in the metabasalt–serpentinite shallow aquifer of mt. reventino (CZ, Italy) by reaction path modelling. *Applied Geochemistry*, *26*(9), 1722-1740. https://doi.org/10.1016/j.apgeochem.2011.04.028

Apte, A. D., Verma, S., Tare, V., & Bose, P. (2005). Oxidation of Cr(III) in tannery sludge to Cr(VI): Field observations and theoretical assessment. *Journal of Hazardous Materials*, *121*(1), 215-222.

Bai, X., & Fan, Z. (2009). Determination of chromium (III) in natural water samples utilizing capillary micro-extraction on nanometre zirconium phosphate coating coupled to electrothermal atomic absorbance spectrometry. *Journal of Environmental Monitoring*, *11*(2), 326-329. https://doi.org/10.1039/B812288A

Ball, J. W., & Izbicki, J. (2004). Occurrence of hexavalent chromium in ground water in the western mojave desert, California. *Applied Geochemistry*, *19*(7), 1123-1135. https://doi.org/10.1016/j.apgeochem.2004.01.011

Barnes, I., & O'Neil, J. R. (1978). Present day serpentinization in New Caledonia, Oman and Yugoslavia. *Geochimica et Cosmochimica Acta*, 42, 144-145. https://doi.org/10.1016/0016-7037(78)90225-9

Bethke, C. M. (2007). *Geochemical and biogeochemical reaction modeling*, Cambridge, UK: Cambridge University Press.

Boschetti, T., & Toscani, L. (2008). Springs and streams of the Taro–Ceno valleys (northern apennine, Italy): Reaction path modeling of waters interacting with serpentinized ultramafic rocks. *Chemical Geology*, *257*(1), 76-91. https://doi.org/10.1016/j.chemgeo.2008.08.017

Bourotte, C., Bertolo, R., Almodovar, M., & Hirata, R. (2009). Natural occurrence of hexavalent chromium in a sedimentary aquifer in Urânia, state of São Paulo, Brazil. *Anais Da Academia Brasileira De Ciências*, *81*(2), 227-242. http://dx.doi.org/10.1590/S0001-37652009000200009

Bruni, J., Canepa, M., Chiodini, G., Cioni, R., Cipolli, F., Longinelli, A., et al. (2002). Irreversible water–rock mass transfer accompanying the generation of the neutral, Mg–HCO 3 and high-pH, Ca–OH spring waters of the Genova province, Italy. *Applied Geochemistry*, *17*(4), 455-474. https://doi.org/10.1016/S0883-2927(01)00113-5

Carrera, J., & Neuman, S. P. (1986) Estimation of aquifer parameters under steady-state and transient condition: 2. Uniqueness, stability, and solution algorithms. *Water Resources Research*, *22*(2), 211-227. https://doi.org/10.1029/WR022i002p00211

Censi, P., Tamburo, E., Speziale, S., Zuddas, P., Randazzo, L., Punturo, R., et al. (2011). Yttrium and lanthanides in human lung fluids, probing the exposure to atmospheric fallout. *Journal of Hazardous Materials*, *186*(2), 1103-1110. https://doi.org/10.1016/j.jhazmat.2010.11.113

Cipolli, F., Gambardella, B., Marini, L., Ottonello, G., & Zuccolini, M. V. (2004). Geochemistry of high-pH waters from serpentinites of the Gruppo di Voltri (Genova, Italy) and reaction path modeling of CO2 sequestration in serpentinite aquifers. *Applied Geochemistry*, *19*(5), 787-802.
https://doi.org/10.1016/j.apgeochem.2003.10.007

Ciriello, V., A. Guadagnini, V. Di Federico, Y. Edery, and B. Berkowitz (2013a), Comparative analysis of formulations for conservative transport in porous media through sensitivity-based parameter calibration, *Water Resources. Research., 49*, 5206-5220.
https://doi.org/10.1002/wrcr.20395.

Ciriello, V., V. Di Federico, M. Riva, F. Cadini, J. De Sanctis, E. Zio, and A. Guadagnini (2013b), Polynomial Chaos Expansion for Global Sensitivity Analysis applied to a model of radionuclide migration in a randomly heterogeneous aquifer. *Stochastic Environmental Research. Risk Assessment*, *27*, 945-954.
https://doi.org/10.1007/s00477-012-0616-7.

Ciriello, V., Y. Edery, A. Guadagnini, and B. Berkowitz (2015), Multimodel framework for characterization of transport in porous media. *Water Resources Research*., *51*(5), 3384-3402.
https://doi.org/10.1002/2015WR017047.

Crawford, J. (1999). *Geochemical Modelling–A review of current capabilities and future directions*, Stockholm, SE: Swedish Environmental Protection Agency.

Dai, Z., & Samper, J. (2004). Inverse problem of multicomponent reactive chemical transport in porous media: Formulation and Applications. *Water Resources Research*, 40,
https://doi.org/10.1029/2004WR003248

Delany, J., & Lundeen, S. (1991). *The LLNL thermochemical database* (Report UCRL-21658), Livermore, CA: Lawrence Livermore National Laboratory.

Dell'Oca, A., Riva, M., & Guadagnini, A. (2017). Moment-based metrics for global sensitivity analysis of hydrological systems. *Hydrology and Earth System Sciences, 21*(12), 6219.
https://doi.org/10.5194/hess-21-6219-2017

Fantoni, D., Brozzo, G., Canepa, M., Cipolli, F., Marini, L., Ottonello, G., & Zuccolini, M. (2002). Natural hexavalent chromium in groundwater interacting with ophiolitic rocks. *Environmental Geology*, *42*(8), 871-882.
https://doi.org/10.1007/s00254-002-0605-0

Fendorf, S. E. (1995). Surface reactions of chromium in soils and waters. *Geoderma*, *67*(1-2), 55-71.
https://doi.org/10.1016/0016-7061(94)00062-F

Fendorf, S., Wielinga, B. W., & Hansel, C. M. (2000). Chromium transformations in natural environments: The role of biological and abiological processes in chromium (VI) reduction. *International Geology Review*, *42*(8), 691-701.
https://doi.org/10.1080/00206810009465107

Ferretti, F., Saltelli , A., & Tarantola, S. (2016). Trends in sensitivity analysis practice in the last decade. *Science of the Total Environment, 568*, 666-670.
https://doi.org/10.1016/j.scitotenv.2016.02.133

Formaggia, L., Guadagnini, A., Imperiali, I., Lever, V., Porta, G., Riva, M., et al. (2013). Global sensitivity analysis through polynomial chaos expansion of a basin-scale geochemical compaction model. *Computational Geosciences, 17*(1), 25-42. https://doi.org/10.1007/s10596-012-9311-5

Garrels, R. M., & Mackenzie, F. T. (1967). Origin of the chemical compositions of some springs and lakes. In W. Stumm (Eds.), *Equilibrium concepts in natural water systems* (vol. 67, pp. 222-242). Washington, DC: Advances in Chemistry, American Chemical Society.

Gray, D. J. (2003). Naturally occurring Cr6 in shallow groundwater of the Yilgarn craton, Western Australia. *Geochemistry: Exploration, Environment, Analysis, 3*(4), 359-368. https://doi.org/10.1144/geochem2014-333

Helgeson, H. C. (1968). Evaluation of irreversible reactions in geochemical processes involving minerals and aqueous solutions—I. thermodynamic relations. *Geochimica et Cosmochimica Acta, 32*(8), 853-877. https://doi.org/10.1016/0016-7037(68)90100-2

Helgeson, H. C., Brown, T. H., Nigrini, A., & Jones, T. A. (1970). Calculation of mass transfer in geochemical processes involving aqueous solutions. *Geochimica et Cosmochimica Acta, 34*(5), 569-592. https://doi.org/10.1016/0016-7037(70)90017-7

Helgeson, H. C., Garrels, R. M., & MacKenzie, F. T. (1969). Evaluation of irreversible reactions in geochemical processes involving minerals and aqueous solutions—II. applications. *Geochimica et Cosmochimica Acta, 33*(4), 455-481. https://doi.org/10.1016/0016-7037(69)90127-6

Iooss, B., & Lemaître, P. (2015). A review on global sensitivity analysis methods. In G. Dellino, C. Meloni (Eds.), *Uncertainty management in simulation-optimization of complex systems* (pp. 101-122). New York, NY: Springer.

Ivarsson, M., Broman, C., & Holm, N. G. (2011). Chromite oxidation by manganese oxides in subseafloor basalts and the presence of putative fossilized microorganisms. *Geochemical Transactions, 12*(1), 5. https://doi.org/10.1186/1467-4866-12-5

Jacobs, J. A., & Testa, S. M. (2005). Overview of chromium (VI) in the environment: Background and history. In J. Guertin, J. A. Jacobs, C. P. Avakian (Eds.), *Chromium (VI) Handbook* (pp. 1-21). Boca Raton, FL: CRC Press.

Kaprara, E., Kazakis, N., Simeonidis, K., Coles, S., Zouboulis, A., Samaras, P., & Mitrakas, M. (2015). Occurrence of Cr (VI) in drinking water of Greece and relation to the geological background. *Journal of Hazardous Materials, 281*, 2-11. https://doi.org/10.1016/j.jhazmat.2014.06.084

Kazakis, N., Kantiranis, N., Kalaitzidou, K., Kaprara, M., Mitrakas, M., Frei, R., Filippidis, A. (2017). Origin of hexavalent chromium in groundwater: The example of Sarigkiol basin, northern Greece. *Science of the Total Environment, 593*, 552-566. https://doi.org/10.1016/j.scitotenv.2017.03.128

Kazakis, N., Kantiranis, N., Voudouris, K., Mitrakas, M., Kaprara, E., & Pavlou, A. (2015). Geogenic Cr oxidation on the surface of mafic minerals and the hydrogeological conditions influencing hexavalent chromium concentrations in groundwater. *Science of the Total Environment, 514*, 224-238. https://doi.org/10.1016/j.scitotenv.2015.01.080

Lelli, M., Grassi, S., Amadori, M., & Franceschini, F. (2013). Natural Cr (VI) contamination of groundwater in the Cecina coastal area and its inner sectors (Tuscany, Italy). *Environmental Earth Sciences, 71*(9), 3907-3919. https://doi.org/10.1007/s12665-013-2776-2

Lin, C. (2002). The chemical transformations of chromium in natural waters–a model study. *Water, Air, & Soil Pollution, 139*(1), 137-158. https://doi.org/10.1023/A:1015870907389

Marini, L. (2013). Reaction path modeling: Theoretical aspects and applications. In P. Censi, Y. Erel. T. Darrah, *Medical geochemistry* (pp. 47-66), New York, NY: Springer.

McClain, C. N., Fendorf, S., Webb, S. M., & Maher, K. (2017). Quantifying Cr(VI) production and export from serpentine soil of California Coast Range. *Environmental Science and Technology*, *51*(1), 141-149.

Mills, C. T., Morrison, J. M., Goldhaber, M. B., & Ellefsen, K. J. (2011). Chromium (VI) generation in vadose zone soils and alluvial sediments of the southwestern Sacramento valley, California: A potential source of geogenic Cr (VI) to groundwater. *Applied Geochemistry, 26*(8), 1488-1501. https://doi.org/10.1016/j.apgeochem.2011.05.023

Morrill, P. L., Kuenen, J. G., Johnson, O. J., Suzuki, S., Rietze, A., Sessions, A. L., et al. (2013). Geochemistry and geobiology of a present-day serpentinization site in California: The cedars. *Geochimica et Cosmochimica Acta, 109*, 222-240. https://doi.org/10.1016/j.gca.2013.01.043

Motzer, W. E., & Engineers, T. (2004). Chemistry, geochemistry, and geology of chromium and chromium compounds. In J. Guertin, J. A. Jacobs, C. P. Avakian (Eds.), *Chromium (VI) Handbook* (pp. 23-88). Boca Raton, FL: CRC Press.

Neuman, S. P. (2003a). Maximum likelihood bayesian averaging of uncertain model predictions. *Stochastic Environmental Research and Risk Assessment, 17*(5), 291-305. https://doi.org/10.1007/s00477-003-0151-7

Neuman, S. P. (2003b). *A Comprehensive Strategy of Hydrogeologic Modeling and Uncertainty Analysis for Nuclear Facilities and Sites*, Washington, DC: Nuclear Regulatory Commission Office of Nuclear Regulatory Research.

Oze, C., Fendorf, S., Bird, D. K., & Coleman, R. G. (2004). Chromium geochemistry of serpentine soils. *International Geology Review, 46*(2), 97-126. https://doi.org/10.2747/0020-6814.46.2.97

Palandri, J. L., & Reed, M. H. (2004). Geochemical models of metasomatism in ultramafic systems: Serpentinization, rodingitization, and sea floor carbonate chimney precipitation. *Geochimica et Cosmochimica Acta, 68*(5), 1115-1133. https://doi.org/10.1016/j.gca.2003.08.006

Panettiere, P., Cortecci, G., Dinelli, E., Bencini, A., & Guidi, M. (2000). Chemistry and sulfur isotopic composition of precipitation at Bologna, Italy. *Applied Geochemistry, 15*(10), 1455-1467. https://doi.org/10.1016/S0883-2927(00)00012-3

Parkhurst D. L. & Appelo C. (2013). *Description of input and examples for PHREEQC version 3—a computer program for speciation, batch-reaction, one-dimensional transport, and inverse geochemical calculations*, Reston, VA: U.S. Department of the Interior, U.S .Geological Survey.

Rakovec, O., Hill, M. C., Clark, M., Weerts, A., Teuling, A., & Uijlenhoet, R. (2014). Distributed evaluation of local sensitivity analysis (DELSA), with application to hydrologic models. *Water Resources Research, 50*(1), 409-426. https://doi.org/10.1002/2013WR014063

Razavi, S., & Gupta, H. V. (2015). What do we mean by sensitivity analysis? the need for comprehensive characterization of "global" sensitivity in earth and environmental systems models. *Water Resources Research, 51*(5), 3070-3092. https://doi.org/10.1002/2014WR016527

Riva, M., Guadagnini, A., & Dell'Oca, A. (2015). Probabilistic assessment of seawater intrusion under multiple sources of uncertainty. *Advances in Water Resources, 75*, 93-104. https://doi.org/10.1016/j.advwatres.2014.11.002

Robles-Camacho, J., & Armienta, M. (2000). Natural chromium contamination of groundwater at Leon valley, Mexico. *Journal of Geochemical Exploration, 68*(3), 167-181. https://doi.org/10.1016/S0375-6742(99)00083-7

Runnells, D. D., Shepherd, T. A., & Angino, E. E. (1992). Metals in water. Determining natural background concentrations in mineralized areas. *Environmental Science & Technology, 26*(12), 2316-2323. https://doi.org/10.1021/es00036a001

Saltelli, A., Ratto, M., Andres, T., Campolongo, F., Cariboni, J., Gatelli, D. et al. (2008). *Global sensitivity analysis: The primer*. Chichester, UK: John Wiley & Sons.

Saltelli, A., Ratto, M., Tarantola, S., & Campolongo, F. (2005). Sensitivity analysis for chemical models. *Chemical Reviews, 105*(7), 2811-2828. https://doi.org/10.1021/cr040659d

Saltelli, A., Ratto, M., Tarantola, S., & Campolongo, F., (2012). Sensitivity analysis for chemical models. *Chemical Reviews 112(*5*)*, PR1–PR21 (Review). https://doi.org/10.1021/cr200301u

Saputro, S., Yoshimura, K., Matsuoka, S., Takehara, K., Aizawa, J., & Tennichi, Y. (2014). Speciation of dissolved chromium and the mechanisms controlling its concentration in natural water. *Chemical Geology, 364*, 33-41. https://doi.org/10.1016/j.chemgeo.2013.11.024

Schott, J., Oelkers, E. H., Bénézeth, P., Goddéris, Y., & François, L. (2012). Can accurate kinetic laws be created to describe chemical weathering? *Comptes Rendus Geoscience, 344*(11), 568-585. https://doi.org/10.1016/j.crte.2012.10.005

Styles, M., Sanna, A., Lacinska, A., Naden, J., & Maroto-Valer, M. (2014). The variation in composition of ultramafic rocks and the effect on their suitability for carbon dioxide sequestration by mineralization following acid leaching. *Greenhouse Gases: Science and Technology, 4*(4), 440-451. https://doi.org/10.1002/ghg.1405

Tartakovsky, D. (2013) Assessment and management of risk in subsurface hydrology: A review and perspective. *Advances in Water Resources, 51*, 247-260. https://doi.org/10.1016/j.advwatres.2012.04.007

Taunton, A. E., Gunter, M. E., Druschel, G. K., & Wood, S. A. (2010). Geochemistry in the lung: Reaction-path modeling and experimental examination of rock-forming minerals under physiologic conditions. *American Mineralogist, 95*(11), 1624-1635.
https://doi.org/10.2138/am.2010.3434

Vengosh, A., Coyte, R., Karr, J., Harkness, J. S., Kondash, A. J., Ruhl, L. S., et al. (2016). Origin of hexavalent chromium in drinking water wells from the piedmont aquifers of North Carolina. *Environmental Science & Technology Letters, 3*(12), 409-414.
https://doi.org/10.1021/acs.estlett.6b00342

Wood, S. A., Taunton, A. E., Normand, C., & Gunter, M. E. (2006). Mineral-fluid interaction in the lungs: Insights from reaction-path modeling. *Inhalation Toxicology, 18*(12), 975-984.
https://doi.org/10.1080/08958370600835252

Yang, C., Dai, Z., Romanak, K., Hovorka, S., & Trevino, R. (2014). Inverse Modeling of Water-Rock-CO2 Batch Experiments: Implications for Potential Impacts on Groundwater Resources at Carbon Sequestration Sites. Environmental Science & Technology, *48* (5), 2798-2806.

Ye, M., Neuman, S.P., Meyer, P.D., Pohlmann, K.F. (2005). Sensitivity analysis and assessment of prior model probabilities in MLBMA with application to unsaturated fractured tuff. *Water Resources Research*, 41.
https://doi.org/10.1029/2005WR004260

Zhu, C., & Anderson, G. (2002). *Environmental applications of geochemical modeling*. Cambridge, UK: Cambridge University Press.

Table 1: Speciation of the meteoric water which constitutes the only recharge of the hydrogeological system outlined in Figure 1. The speciation is obtained following the procedure proposed by *Boschetti and Toscani* (2008).

Table 2: Mineral phases composing the partially altered *Cr*-rich ophiolitic outcrop.

Table 3: Secondary phases allowed to precipitate downstream of the meteoric water and ophiolitic rock interaction.

Table 4: Ranges of variability selected for each parameter describing the environmental conditions of the flowing path.

Table 1: Speciation of the meteoric water which constitutes the only recharge of the hydrogeological system outlined in Figure 1. The speciation is obtained following the procedure proposed by *Boschetti and Toscani* (2008).

Element/Quantity	Molality [mol Kg^{-1}]	Element/Quantity	Molality [mol Kg^{-1}]
Al	1.35×10^{-6}	*Mg*	1.2×10^{-5}
C	5.8×10^{-5}	*N*	3.7×10^{-5}
Ca	7.7×10^{-5}	*Na*	3.5×10^{-5}
Cl	3.9×10^{-5}	*S*	3.5×10^{-5}
Fe	1.3×10^{-8}	*Si*	1.35×10^{-6}
K	1.1×10^{-5}	*pH*	5.4

Table 2: Mineral phases composing the partially altered *Cr*-rich ophiolitic outcrop.

Phases	Molar percentage [%]	Thermodynamic data reference
Al-lizardite ($Mg_{2.7}Fe_{0.2}Al_{0.2}Si_{1.9}O_5(OH)_4$)	86	*Boschetti and Toscani* (2008)
Chromite ($FeCr_2O_4$)	1	LLNL Database
Chrysotile ($Mg_3Si_2O_5(OH)_4$)	5	LLNL Database
Clinochlore-daphnite ($Mg_4FeAl_2Si_3O_{10}(OH)_8$)	2	LLNL Database
Magnetite (Fe_3O_4)	1	LLNL Database
Spinel (Al_2MgO_4)	1	LLNL Database
Albite ($NaAlSi_3O_8$)	1	LLNL Database
Anorthite ($CaAl_2(SiO_4)_2$)	3	LLNL Database

Table 3: Secondary mineral phases allowed to precipitate as a consequence of ophiolites weathering.

Phases		**Composition**	**Thermodynamic data reference**
Kaolinite		$Al_2Si_2O_5(OH)_4$	LLNL database
Gibbsite		$Al(OH)_3$	LLNL database
Hydromagnesite		$Mg_5(CO_3)_4(OH)_2{:}4H_2O$	LLNL database
Brucite		$Mg(OH)_2$	LLNL database
Nesquehonite		$MgCO_3{:}3H_2O$	LLNL database
Ideal solid solution of Montmorillonites:			
	Mg-montmorillonite	$Mg_{.495}Al_{1.67}Si_4O_{10}(OH)_2$	LLNL database
	K-montmorillonite	$K_{.33}Mg_{.33}Al_{1.67}Si_4O_{10}(OH)_2$	LLNL database
	Ca-montmorillonite	$Ca_{.165}Mg_{.33}Al_{1.67}Si_4O_{10}(OH)_2$	LLNL database
	Na-montmorillonite	$Na_{.33}Mg_{.33}Al_{1.67}Si_4O_{10}(OH)_2$	LLNL Database
	Mn(II)-montmorillonite	$Mn_{.165}Mg_{.33}Al_{1.67}Si_4O_{10}(OH)_2$	*Fantoni et al.* (2002)
	Mn(III)-montmorillonite	$Mn_{.11}Mg_{.33}Al_{1.67}Si_4O_{10}(OH)_2$	*Fantoni et al.* (2002)
	Cr(III)-montmorillonite	$Cr_{.11}Mg_{.33}Al_{1.67}Si_4O_{10}(OH)_2$	*Fantoni et al.* (2002)
	Ni-montmorillonite	$Ni_{.165}Mg_{.33}Al_{1.67}Si_4O_{10}(OH)_2$	*Fantoni et al.* (2002)
	Fe(II)-montmorillonite	$Fe_{.165}Mg_{.33}Al_{1.67}Si_4O_{10}(OH)_2$	*Fantoni et al.* (2002)
	Fe(III)-montmorillonite	$Fe_{.11}Mg_{.33}Al_{1.67}Si_4O_{10}(OH)_2$	*Fantoni et al.* (2002)
Ideal solid solution of Carbonates:			
	Calcite	$CaCO_3$	LLNL Database
	Siderite	$FeCO_3$	LLNL Database
	Rhodocrosite	$MnCO_3$	LLNL Database
Ideal solid solution of Hydroxides			
	Fe(II)-hydroxide	($Fe(OH)_2$)	LLNL Database
	Fe(III)-hydroxide	($Fe(OH)_3$)	LLNL Database
	amorphous *Mn(II)*-hydroxide	($Mn(OH)_2$)	LLNL Database
	Mn(III)-hydroxide	($Mn(OH)_3$)	LLNL Database
	Ni-hydroxide	($Ni(OH)_2$)	LLNL Database
	Cr(III)-hydroxide	($Cr(OH)_3$)	LLNL Database
Ideal solid solution of Saponites			
	Ca-saponite	$Ca_{.165}Mg_3Al_{.33}Si_{3.67}O_{10}(OH)_2$	LLNL Databasa
	K-saponite	$K_{.33}Mg_3Al_{.33}Si_{3.67}O_{10}(OH)_2$	LLNL Database
	Mg-saponite	$Mg_{3.165}Al_{.33}Si_{3.67}O_{10}(OH)_2$	LLNL Database
	Na-saponite	$Na_{.33}Mg_3Al_{.33}Si_{3.67}O_{10}(OH)_2$	LLNL Database
	Fe(III)-saponite	$Fe_{.11}Mg_3Al_{.33}Si_{3.67}O_{10}(OH)_2$	*Fantoni et al.* (2002)
	Fe(II)-saponite	$Fe_{.165}Mg_3Al_{.33}Si_{3.67}O_{10}(OH)_2$	*Fantoni et al.* (2002)
	Cr(III)-saponite	$Cr_{.11}Mg_3Al_{.33}Si_{3.67}O_{10}(OH)_2$	*Fantoni et al.* (2002)
	Mn(II)-saponite	$Mn_{.165}Mg_3Al_{.33}Si_{3.67}O_{10}(OH)_2$	*Fantoni et al.* (2002)
	Mn(III)-saponite	$Mn_{.11}Mg_3Al_{.33}Si_{3.67}O_{10}(OH)_2$	*Fantoni et al.* (2002)
	Ni-saponite	$Ni_{.165}Mg_3Al_{.33}Si_{3.67}O_{10}(OH)_2$	*Fantoni et al.* (2002)

Figure 1: The simplified hydrogeological setting studied in this work. The water path is segmented into three main phases: (*i*) meteoric water infiltrates into the subsurface; (*ii*) water flows in the subsurface fracture network and then (*iii*) gushes out as springs.

Figure 2: Scatter plots obtained for *N* realizations of: log *Cr*(*VI*) corresponding to the *N* samples of (a) log f_{O2}, (b) log f_{CO2}, and (c) *T*; –log H^+ values (i.e., *pH*) corresponding to the *N* samples of (d) log f_{O2}, (e) log f_{CO2}, and (f) *T*. Each panel depicts the scatters plots corresponding to three ξ steps, i.e. $\xi_1 = 1\times10^{-8}$ mol (black circles), $\xi_2 = 1\times10^{-4}$ mol (red circles), and $\xi_3 = 0.5$ mol (blue circles).

Figure 3: Evolution of $\left\langle SL_{f_{O2}} \right\rangle^i$ as a function of log f_{O2} and the reaction progress variable ξ for (a) *Cr(VI)*, and (b) *Cr(III)* molalities. The shadowed blue and green areas indicate the sub-region of Θ_1 where *Cr(III)* and *Cr(VI)* can respectively be considered as the dominant valence state in the system. The dashed grey curves correspond to $\left\langle SL_{f_{O2}} \right\rangle^i + std$ (where *std* is the standard deviation of $\left\langle SL_{f_{O2}} \right\rangle^i$).

Figure 4: distribution in the parameter space of the local indices $SL_{f_{O2}}$ (panels (a) and (d)), $SL_{f_{CO2}}$ (panels (b) and (e)), and SL_T (panels(c) and (f)) as defined by the DELSA analysis for the target variable H^+ at two diverse progress variable steps $\xi = 0.5$ mol (panels (a), (b) and (c)) and $\xi = 1\times10^{-8}$ mol (panels (d), (e) and (f)).

Figure 5: Evolution of $\left\langle SL_{f_{O2}} \right\rangle^i$ as a function of log f_{O2} and the reaction progress variable ξ for (a) H^+ and (b) *C* molalities. The shadowed yellow and red areas respectively indicate the sub-region of Θ_1 where *Cr* and *N* change their dominant valence state. Dashed grey curves correspond to $\left\langle SL_{f_{O2}} \right\rangle^i \pm std$ (where *std* is the standard deviation of $SL_{f_{O2}}$).

Figure 6: MM-GSA indices computed for H^+. Index *AMAE* computed at ξ = (a) 1×10^{-8} mol, (b) 1×10^{-4} mol, and (c) 0.5 mol for log f_{O2} (blue), log f_{CO2}(red), and *T* (black). Index *AMAV* computed at ξ = (d) 1×10^{-8} mol, (e) 1×10^{-4} mol, and (f) 0.5 mol for log f_{O2} (blue), log f_{CO2}(red), and *T* (black). In all panels the indices *AMAE* and *AMAV* are computed relying on all the realizations sampled in Ω (dashed horizontal lines) or relying only on region-specific realizations, i.e., parameter realizations associated with each of the intervals I_w (w = 1, ... ,5, filled circles) defined in Section 4.1.3 and identified as shaded areas in the figure.

Figure 7: MM-GSA indices computed for (a), (c) *Cr(III)*, and (b), (d) *Cr(VI)*. Index (a), (b) *AMAE* and (c), (d) *AMAV* are computed at $\xi = 0.5 mol$ for log f_{O2} (blue), log f_{CO2}(red) and *T* (black). In all panels the indices *AMAE* and *AMAV* are computed relying on all the realizations sampled in Ω (dashed horizontal lines) or relying only on region-specific realizations, i.e., parameter realizations associated with each of the intervals I_w (w = 1, ... ,5, filled circles) defined in Section 4.1.3 and identified as shaded areas in the figure.

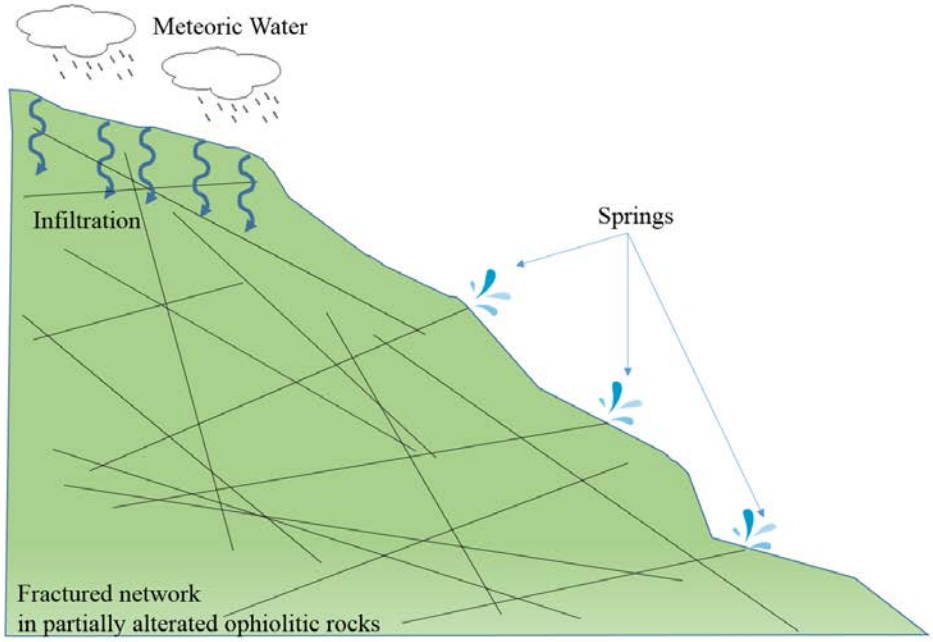

Figure 1: The simplified hydrogeological setting studied in this work. The water path is segmented into three main phases: (*i*) meteoric water infiltrates into the subsurface; (*ii*) water flows in the subsurface fracture network and then (*iii*) gushes out as springs.

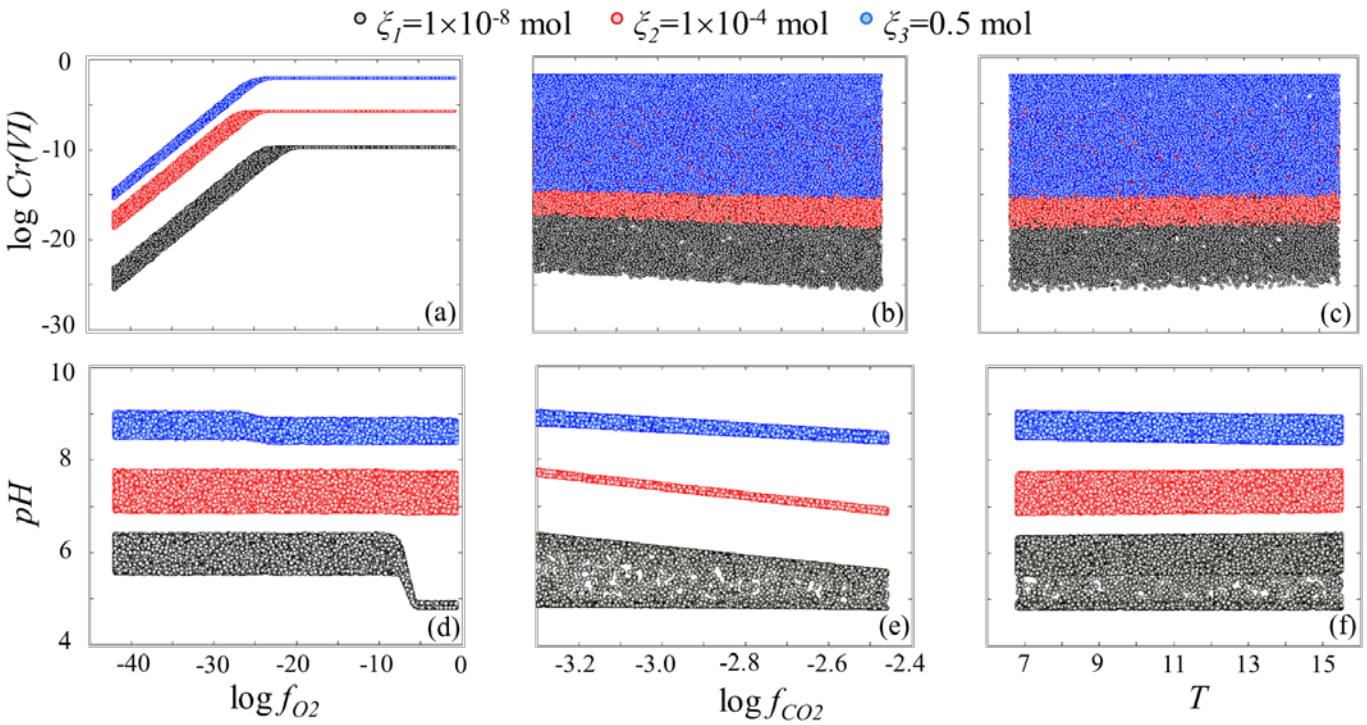

Figure 2: Scatter plots obtained for N realizations of: log $Cr(VI)$ corresponding to the N samples of (a) log f_{O2}, (b) log f_{CO2}, and (c) T; –log H^+ values (i.e., pH) corresponding to the N samples of (d) log f_{O2}, (e) log f_{CO2}, and (f) T. Each panel depicts the scatters plots corresponding to three ξ steps, i.e. ξ_1 =1×10^{-8} mol (black circles), ξ_2 =1×10^{-4} mol (red circles), and ξ_3 =0.5 mol (blue circles).

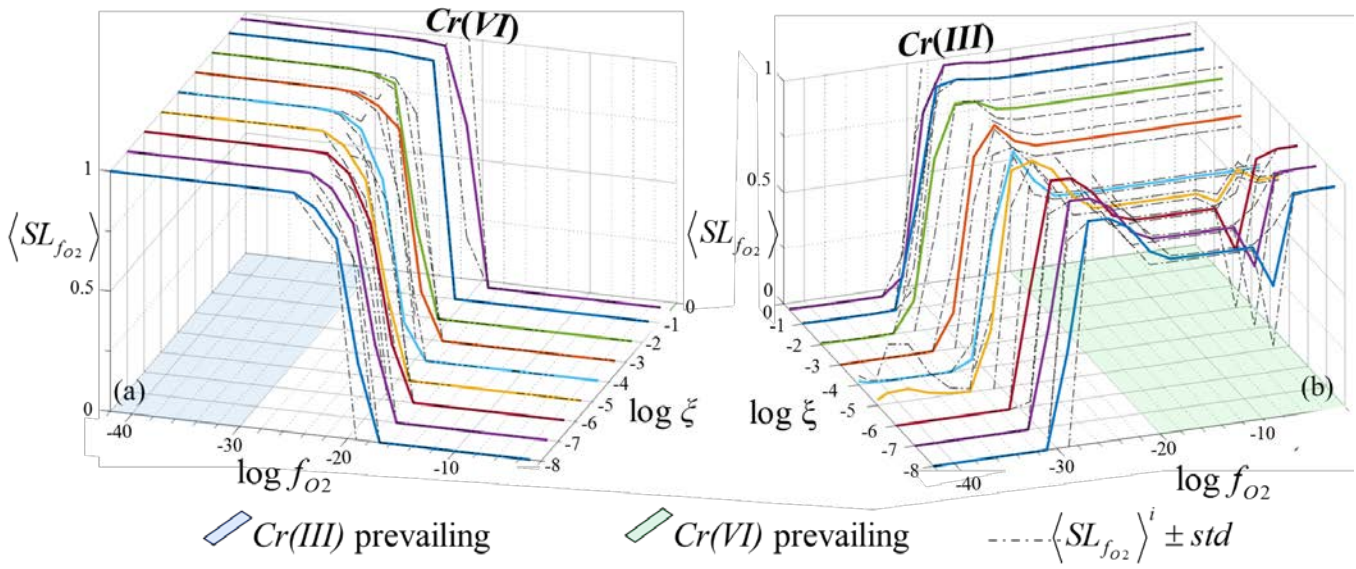

Figure 3: Evolution of $\langle SL_{f_{O2}} \rangle^i$ as a function of log f_{O2} and the reaction progress variable ξ for (a) *Cr(VI)*, and (b) *Cr(III)* molalities. The shadowed blue and green areas indicate the sub-region of Θ_1 where *Cr(III)* and *Cr(VI)* can respectively be considered as the dominant valence state in the system. The dashed grey curves correspond to $\langle SL_{f_{O2}} \rangle^i + std$ (where *std* is the standard deviation of $\langle SL_{f_{O2}} \rangle^i$).

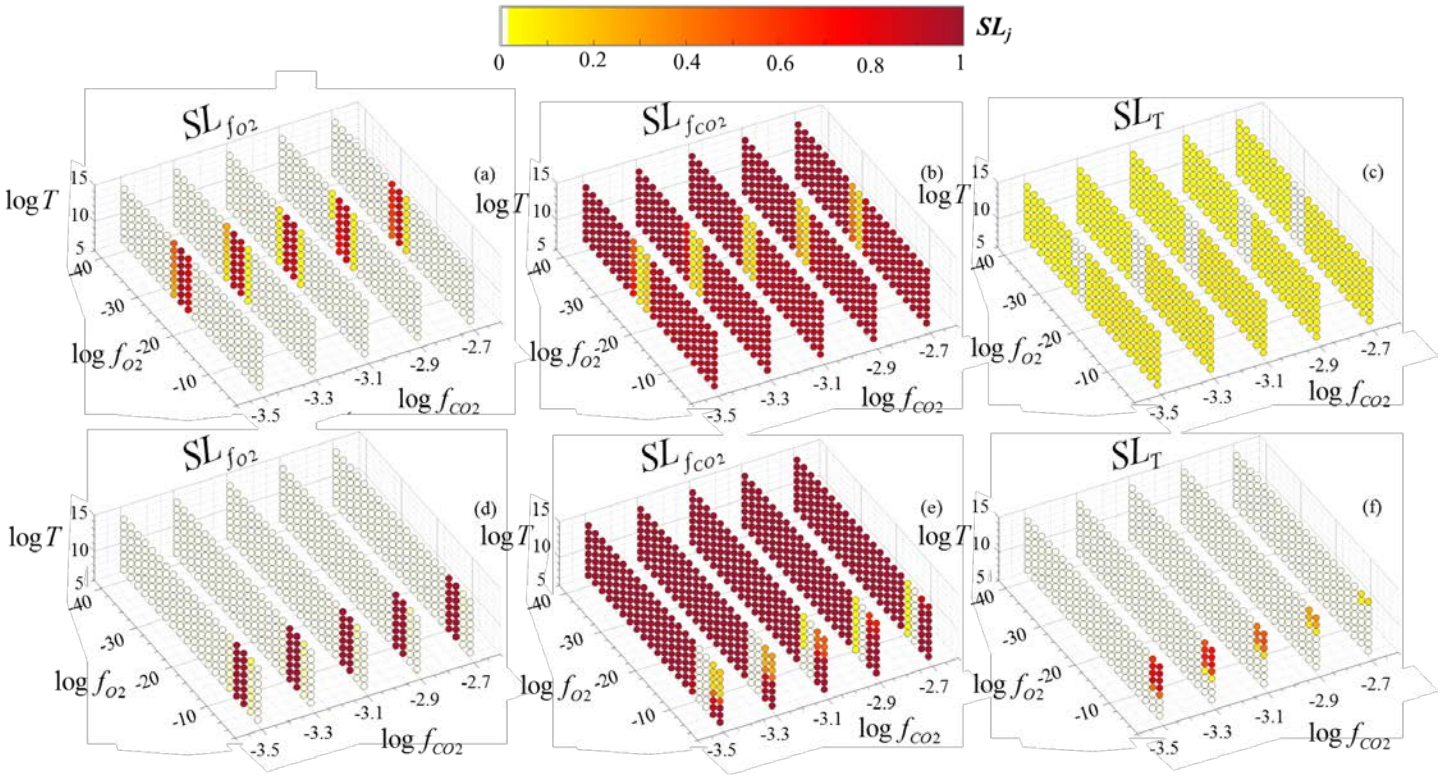

Figure 4: distribution in the parameter space of the local indices $SL_{f_{O2}}$ (panels (a) and (d)), $SL_{f_{CO2}}$ (panels (b) and (e)), and SL_T (panels(c) and (f)) as defined by the DELSA analysis for the target variable H^+ at two diverse progress variable steps $\xi = 0.5$ mol (panels (a), (b) and (c)) and $\xi = 1\times10^{-8}$ mol (panels (d), (e) and (f)).

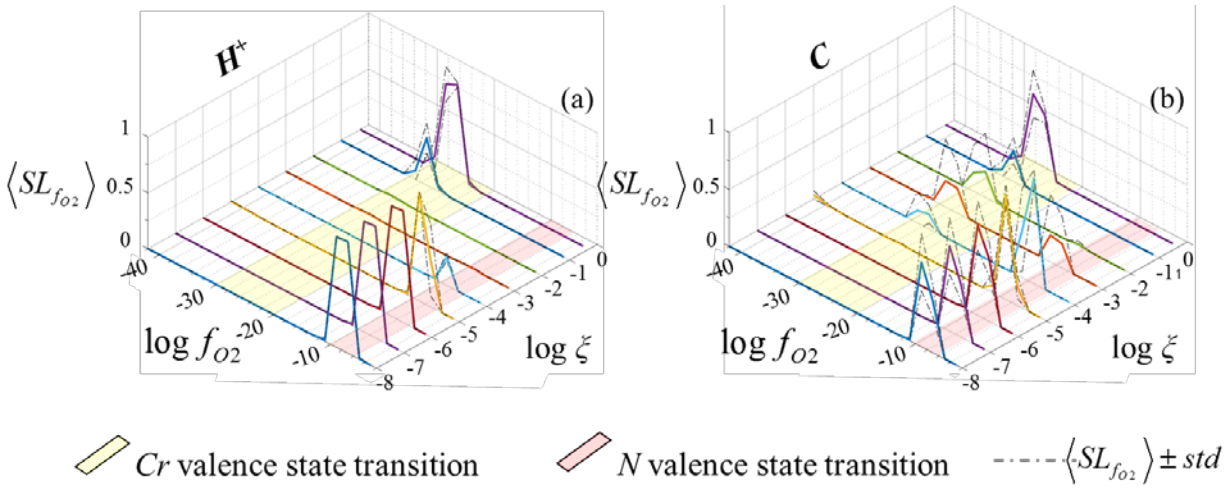

Figure 5: Evolution of $\langle SL_{f_{O2}} \rangle^i$ as a function of log f_{O2} and the reaction progress variable ξ for (a) H^+ and (b) *C* molalities. The shadowed yellow and red areas respectively indicate the sub-region of Θ_1 where *Cr* and *N* change their dominant valence state. Dashed grey curves correspond to $\langle SL_{f_{O2}} \rangle^i \pm std$ (where *std* is the standard deviation of $SL_{f_{O2}}$).

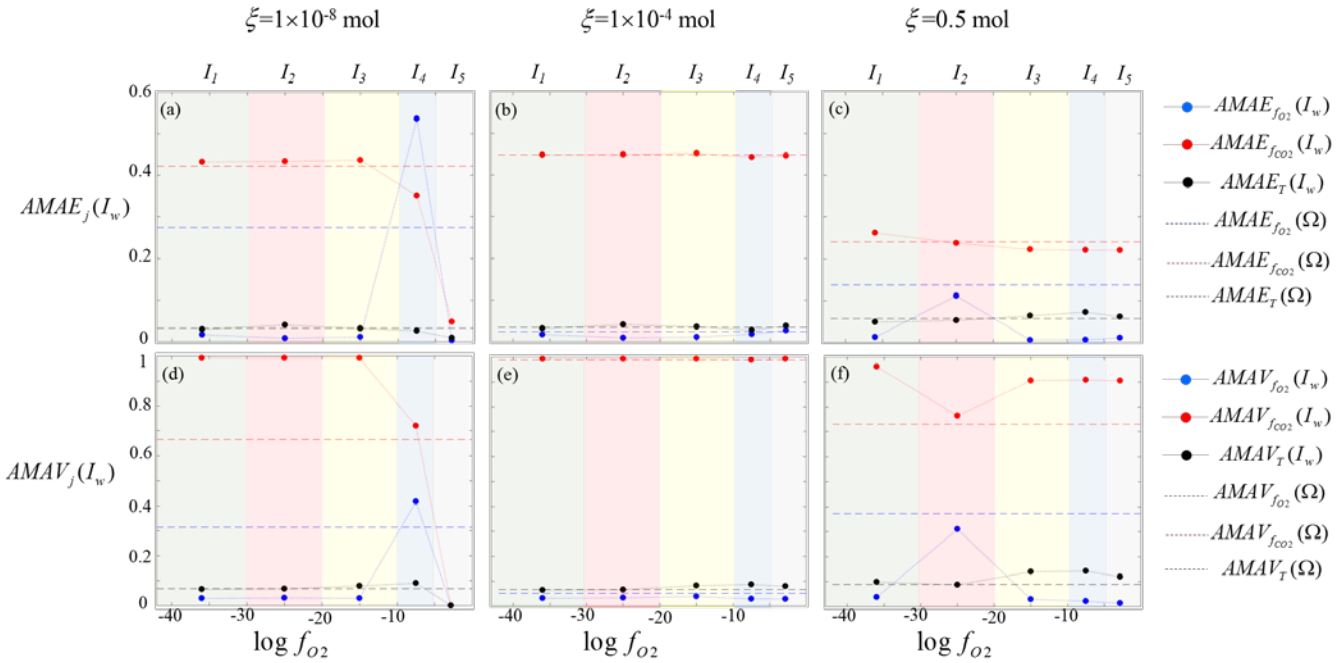

Figure 6: MM-GSA indices computed for H^+. Index *AMAE* computed at ξ = (a) 1×10^{-8} mol, (b) 1×10^{-4} mol, and (c) 0.5 mol for log f_{O2} (blue), log f_{CO2}(red), and T (black). Index *AMAV* computed at ξ = (d) 1×10^{-8} mol, (e) 1×10^{-4} mol, and (f) 0.5 mol for log f_{O2} (blue), log f_{CO2}(red), and T (black). In all panels the indices *AMAE* and *AMAV* are computed relying on all the realizations sampled in Ω (dashed horizontal lines) or relying only on region-specific realizations, i.e., parameter realizations associated with each of the intervals I_w (w = 1, ... ,5, filled circles) defined in Section 4.1.3 and identified as shaded areas in the figure.

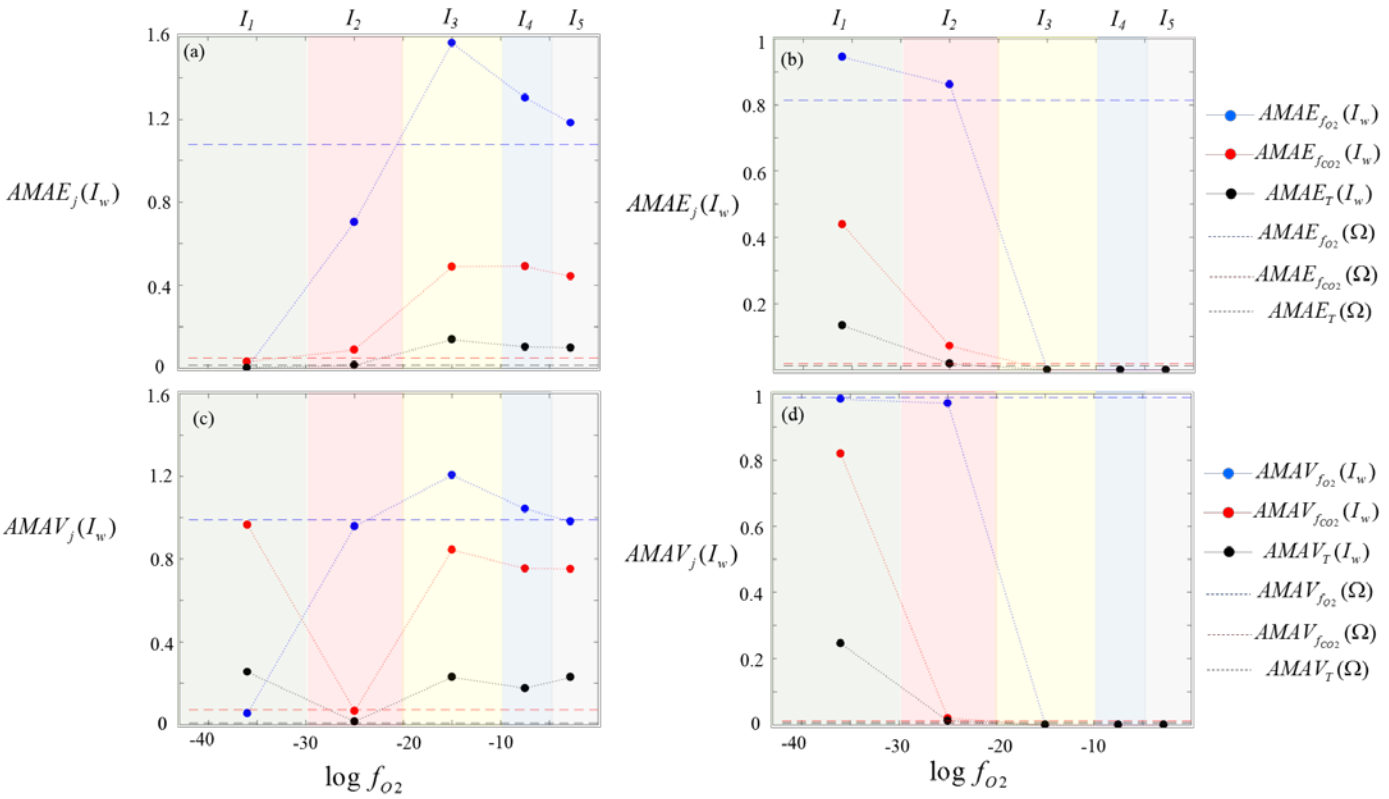

Figure 7: MM-GSA indices computed for (a), (c) *Cr(III)*, and (b), (d) *Cr(VI)*. Index (a), (b) *AMAE* and (c), (d) *AMAV* are computed at $\xi = 0.5 mol$ for log f_{O2} (blue), log f_{CO2}(red) and *T* (black). In all panels the indices *AMAE* and *AMAV* are computed relying on all the realizations sampled in Ω (dashed horizontal lines) or relying only on region-specific realizations, i.e., parameter realizations associated with each of the intervals I_w (w = 1, ... ,5, filled circles) defined in Section 4.1.3 and identified as shaded areas in the figure.

Table 4: Ranges of variability selected for each uncertain model parameter describing the environmental conditions of the flowing path.

Parameter	Lower Bound	Upper Bound
$\log f_{O2}$ (f_{O2} in atm)	-42	-0.67
$\log f_{CO2}$ (f_{CO2} in atm)	-3.5	-1.5
T (°C)	6.8	15.5